Anomalous Tropical Instability Wave Activity Hindered the Development of the 2016/17 La Niña

Aoyun Xue, Wenjun Zhang, Julien Boucharel, Fei-Fei Jin

▶ **To cite this version:**

Anomalous Tropical Instability Wave Activity Hindered the Development of the 2016/17 La Niña

Aoyun Xue,[a] Wenjun Zhang,[a] Julien Boucharel,[b] and Fei-Fei Jin[c]

[a] CIC-FEMD/ILCEC, Key Laboratory of Meteorological Disaster of Ministry of Education, Nanjing University of Information Science and Technology, Nanjing, China
[b] LEGOS, University of Toulouse, CNRS, IRD, CNES, UPS, Toulouse, France
[c] Department of Atmospheric Sciences, SOEST, University of Hawai'i at Mānoa, Honolulu, Hawaii

ABSTRACT: Although the 1997/98 and 2015/16 El Niño events are considered to be the strongest on record, their subsequent La Niña events exhibited contrasted evolutions. In this study, we demonstrate that the extremely strong period of tropical instability waves (TIWs) at the beginning of boreal summer of 2016 played an important role in hindering the subsequent La Niña's development by transporting extra off-equatorial heat into the Pacific cold tongue. By comparing the TIWs' contribution based on an oceanic mixed layer heat budget analysis for the 1998 and 2016 episodes, we establish that TIW-induced nonlinear dynamical heating (NDH) is a significant contributor to the El Niño–Southern Oscillation (ENSO) phase transition in 2016. TIW-induced NDH contributed to around 0.4°C warming per month during the early boreal summer (May–June) following the 2015/16 El Niño's peak, which is found to be an essential inhibiting factor that prevented the subsequent La Niña's growth. A time-mean eddy kinetic energy analysis reveals that anomalous TIWs during 2016 mainly gained their energy from the baroclinic instability conversion due to a strong SST warming in the northeastern off-equatorial Pacific that promoted an increased meridional SST gradient. This highlights the importance of accurately reproducing TIW activity in ENSO simulation and the benefit of off-equatorial SST anomalies in the eastern Pacific as an independent precursor for ENSO predictions.

KEYWORDS: Eddies; La Niña; Heat budgets/fluxes; Instability; Kinetic energy

1. Introduction

As a large-scale coupled ocean–atmospheric instability in the tropical Pacific, El Niño–Southern Oscillation (ENSO) is the most pronounced source of interannual climate variability (e.g., Rasmusson and Carpenter 1982; Wallace et al. 1998; McPhaden et al. 2006). Since ENSO, and in particular super El Niño events, exert profound climate and societal impacts worldwide (e.g., van Loon and Madden 1981; Ropelewski and Halpert 1987, 1996; Trenberth and Caron 2000; Alexander et al. 2002), tremendous efforts have been devoted to understanding ENSO dynamics and improving ENSO forecast skills. The basic physics of the evolution of ENSO are now reasonably well apprehended by the Bjerknes feedback and the simple delayed oscillator/recharge oscillator paradigm (Bjerknes 1969; Battisti and Hirst 1989; Suarez and Schopf 1988; Jin 1997a,b; Weisberg and Wang 1997; Picaut 1997). However, these linear theories cannot account for the spatiotemporal diversity and complexity of ENSO (Timmermann et al. 2018). Therefore, difficulties still remain for accurate ENSO simulations and predictions.

The 1997/98 and 2015/16 El Niño events are considered to be the strongest on record (Levine and McPhaden 2016). Although there were some noteworthy differences between these two events (e.g., Santoso et al. 2017; L'Heureux et al. 2017; Paek et al. 2017; Lim et al. 2017; Kakatkar et al. 2018), they were marked by a fairly similar evolution of sea surface temperature

anomalies (SSTAs) in the equatorial Pacific, both leading to anomalies in the Niño-3.4 region of nearly 2.5°C, as shown in Fig. 1a. However, the two events greatly differed from each other during their decaying phases. After the 2015 El Niño onset, a weak La Niña event materialized as the SST anomalies barely reached the La Niña threshold (http://www.cpc.ncep.noaa. gov/products/analysis_monitoring/enso_disc_dec2016/ensodisc. pdf). Most state-of-the-art dynamical and statistical models also predicted the weak La Niña signals in 2016 very well as Fig. 1b shows, although the predicted intensity exhibits a wide spread across these coupled models. In contrast, the 1998 La Niña event evolved into a relatively strong one characterized by a Niño-3.4 index of 1.5°C below the climatological average. Although the SST imprint for each event was unique, analyzing the differences between these two major episodes and the underlying mechanisms involved is essentially critical to better understand ENSO dynamics. Several studies have compared the evolution and driving processes between the 1997/98 and 2015/16 ENSO events (e.g., Santoso et al. 2017; L'Heureux et al. 2017; Paek et al. 2017; Lim et al. 2017; Li et al. 2019).

Pioneering studies have shown that ENSO events have some useful predictability in advance due to the equatorial heat content recharge/discharge processes in the upper ocean (Cane and Zebiak 1985; Jin 1997a,b; Meinen and McPhaden 2000). Previous study suggested that weak discharge process due to the wind forcing from the year 2015 onward was the primary factor responsible for the weakening of 2016 La Niña, whereas a large discharge after the 1997 El Niño led to a following strong La Niña (Kakatkar et al. 2018). Planton et al. (2018) further
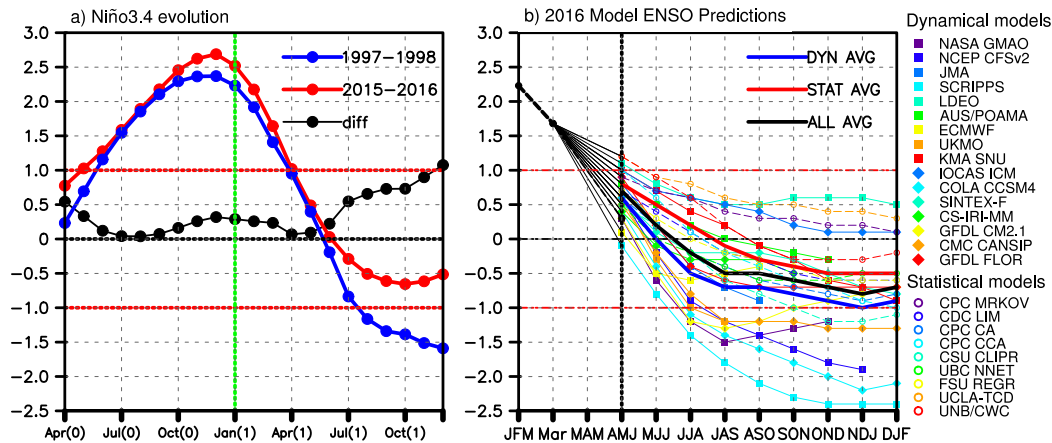
FIG. 1. (a) Time evolution of SST anomalies in the Niño-3.4 region (5°N–5°S, 120°–170°W) for the El Niño/La Niña events of 1997/98 (blue) and 2015/16 (red), and their difference (black). (b) Plume of forecasts of the Niño-3.4 SST anomaly from dynamical and statistical models that were run in mid-April 2016. The average of the forecasts of the dynamical models is shown by the thick blue line, and of the statistical models by the thick red line. The average of all the models is shown by the thick black line.

underlined that the western equatorial Pacific oceanic heat content [warm water volume in the west (WWVw)] is the best ENSO predictor beyond 1-yr lead and a discharged WWVw in boreal fall is a better predictor of La Niña in terms of occurrence and amplitude and consequently could have predicted the weak 2016 La Niña in advance. Yet, these early studies relying on a linear ENSO view could not sufficiently explain the observed La Niña diversity, particularly in terms of the temporal evolution. Some other more complex mechanisms have also been proposed to explain La Niña diversity. For instance, the nonlinear dynamical heating (NDH, i.e., the advection of temperature anomalies by anomalous oceanic currents) at seasonal and interannual time scale has been suggested to be the dominant dynamical source for ENSO asymmetry by enhancing and reducing the amplitude of the warm and cold phases, respectively (Jin et al. 2003; An and Jin 2004). Thus, the NDH could contribute to the observed La Niña diversity. In addition, the meridional movement of associated westerly anomalies and its discharging effect during ENSO decaying phase could also contribute to the ENSO evolution and La Niña amplitude (e.g., Harrison and Vecchi 1999; Vecchi and Harrison 2003, 2006; Vecchi 2006; McGregor et al. 2013). Moreover, the role of extratropical SSTA forcing has been widely argued to play a significant role on ENSO formation and evolution (e.g., Alexander et al. 2010; Zhang et al. 2014a,b; Min et al. 2015, 2017; Paek et al. 2017; Zheng et al. 2015; Zhu et al. 2016; Su et al. 2014, 2018; Wu et al. 2018). For instance, it has been proposed that self-sustaining SSTAs in the northern subtropical Pacific tended to weaken the trade winds during boreal spring–summer in 2016, leading to anomalous westerlies along the equatorial region and hindering La Niña development (Su et al. 2018). The Pacific meridional mode (PMM), characterized by an anomalous north–south SST gradient and anomalous surface circulation in the northeasterly trade regime with maximum variance in boreal spring, is favorable for ENSO development in the following

winter through the seasonal footprinting mechanism (Vimont et al. 2001, 2003a,b; Chiang and Vimont 2004; Chang et al. 2007). Previous studies have noted that a positive PMM could influence ENSO and particularly weakens La Niña by loading the subsurface heat content along the equator through the "trade wind charging" mechanism (TWC) (e.g., Anderson et al. 2013; Amaya 2019; Chakravorty et al. 2020). The important role of Madden–Julian oscillation (MJO) in the termination of El Niño event through the associated ocean upwelling in the eastern equatorial Pacific has also been proposed, which could partially account for the different La Niña evolution (e.g., Miyakawa et al. 2017). Westerly wind events (WWEs) and easterly wind surge (EWS) associated with internal atmospheric variability may also play an important role in generating diverse ENSO behaviors (e.g., Lengaigne et al. 2004; Menkes et al. 2014; Chen et al. 2015; Hu and Fedorov 2016, 2017). The possible influence of the negative IOD at the end of 2015/16 El Niño on the unexpectedly weak La Niña evolution of 2016 also has been explored (Lim and Hendon 2017).

As an oceanic-sourced intraseasonal process, tropical instability waves (TIWs) have not received as much attention as atmospheric processes in influencing the ENSO irregularity and diversity. TIWs are mesoscale wave features that form in the tropical Pacific and Atlantic Oceans along the edge of the cold tongue, with a wavelength of 1000–2000 km and a period of 10–60 days, mostly being observed north of the equator along the SST front with an approximately 33-day period (Legeckis 1977; Weisberg and Weingartner 1988; Qiao and Weisberg 1995). TIWs could be generated by barotropic instability from the meridional shears of the equatorial current system (e.g., Cox 1980; Philander 1976; Im et al. 2012) and baroclinic instability from the meridional SST gradient between the cold tongue and the waters north and south of the equator (e.g., Hansen and Paul 1984; Wilson and Leetmaa 1988; Yu et al. 1995). It has been confirmed that Kelvin–Helmholtz mechanism through vertical shear of ocean current also represents an important energy contribution to the growth

of TIWs (Proehl 1996). Studies show that TIWs influence the characteristics of ENSO by transporting heat into the cold tongue from off-equatorial regions (e.g., An 2008; Bryden and Brady 1989; Imada and Kimoto 2012; Menkes et al. 2006). TIWs act as an asymmetric negative feedback onto ENSO and could partly explain ENSO amplitude asymmetry through NDH (e.g., Vialard et al. 2001; Wang and McPhaden 2001; An and Jin 2004; Jochum and Murtugudde 2006; An 2008; Boucharel and Jin 2020; Xue et al. 2020). It was found that TIWs could also influence ENSO evolution through damping the heat anomalies induced by intraseasonal Kelvin waves, which may decrease the ability of Kelvin waves to kick-start the air–sea feedbacks necessary to initiate ENSO events (Holmes and Thomas 2016).

However, TIWs are often not fully resolved in coarse models (Latif et al. 2001; Graham 2014), which may cause a significant underestimation of SST variability in the central and eastern equatorial Pacific. As an example, it was pointed out that TIW activity is seriously underestimated compared with observations (by a factor of $\sim$3) in the GODAS reanalysis product (Huang et al. 2010; Xue et al. 2020), which could therefore not adequately resolve the associated entrainment of off-equatorial heat into the cold tongue. Indeed, there is some evidence that increasing the horizontal resolution so that realistic TIWs are produced can significantly improve ENSO predictions (Ham and Kang 2011). It was also pointed out that including TIW SST variability in the forcing of an atmospheric model increased wind and rainfall variability near the equator and near $\pm 25°$ latitude by up to 35%, which could potentially contribute to the irregularity of the ENSO cycle (Jochum et al. 2007). Using a hybrid coupled model, Holmes et al. (2019) further examined the impact of TIWs on ENSO irregularity and predictability. However, how such oceanic-sourced intraseasonal variability could influence ENSO characteristics and in particular La Niña diversity is still not clear and needs to be further quantified.

The purpose of this research is mainly to demonstrate that TIW activity plays an overall important role in La Niña diversity through the case study of the 1998/99 and 2016/17 events. In particular, the important role of TIW-induced NDH on the weakening of the 2016/17 event is largely evidenced and quantified. Furthermore, we address the possible physical mechanisms that drive this extreme TIW activity. The remainder of this paper is organized as follows. In section 2, we describe the datasets and definition of TIW indices. We present the comparison of the evolution of two episodes (i.e., 1998/99 and 2016/17 La Niña events) in section 3. In section 4, we compare the intensity of TIW activity and TIW-induced NDH between these two events. In section 5, we explore possible mechanisms that modulate the anomalous TIW activity. The major conclusions are summarized and discussed in section 6.

2. Dataset and methodology

a. Dataset

We used the following observational/reanalysis products: 1) monthly SSTA from the Extended Reconstructed Sea Surface Temperature (ERSST), version 5, from the National Oceanic

and Atmospheric Administration (NOAA) with a resolution of 1° (Huang et al. 2017); 2) the NOAA high-resolution blended analysis of daily Optimum Interpolation Sea Surface Temperature, version 2 (OISSTv2), with a resolution of 1/4° (Reynolds et al. 2002); 3) the ocean three-dimensional reanalysis data from the NCEP Global Ocean Data Assimilation System (GODAS) pentad dataset with a horizontal resolution of 1° longitude and 1/3° latitude, and a vertical resolution of 10 m (Behringer and Xue 2004); and 4) monthly 10-m zonal wind fields from ERA5 atmospheric reanalysis data with a horizontal resolution of 1/4° (Hersbach and Dee 2016). All products used here span from 1980 to 2018, and anomalies were calculated as the departures from the climatological monthly mean over the entire period. Note that the climatological mean for the OISSTv2 data was derived based on the period of 1982–2018 due to the length of the data available.

The Niño-3.4 index is classically used to describe the ENSO intensity and is defined as the area-averaged SST anomalies in the Niño-3.4 region (5°S–5°N, 120°–170°W). The WWVw index used in this study is defined as the area-averaged heat content in the western equatorial Pacific (5°S–5°N, 120°E–155°W) from the Tropical Atmosphere Ocean Project (TAO). The PMM wind index was calculated following the method described in Chiang and Vimont (2004) and downloaded from the website https://www.esrl.noaa.gov/psd/data/timeseries/monthly/PMM. To isolate TIWs and calculate their induced NDH, we apply a 10–60-day Fourier bandpass filter to the GODAS dataset. It should be noted that we use the NOAA OISSTv2 in section 4a to compare the TIW activity between the two episodes. In section 4b, we use the GODAS dataset to calculate the TIW-induced nonlinear oceanic heat flux. In section 4c, we use the combined NOAA and GODAS to quantify the TIW-induced NDH. All statistical significance tests were performed based on the two-tailed Student's t test.

b. Definition of TIW indices

We use the NOAA high-resolution daily SST to define the complex TIW index based on the previous definition by Boucharel and Jin (2020) and Xue et al. (2020). It should be noted that we mainly focus on the TIWs variability characterized by the first meridional Rossby mode with a $\sim$33-day period featured north of the equator along the SST front (e.g., Lyman et al. 2007; Shinoda et al. 2009). The $\sim$17-day period Yanai mode's contribution to TIW activity will not be considered in our present research. Indeed, Yanai wave patterns located south of the equator and mainly in the subsurface ($\sim$100 m depth) indicate a small heat flux convergence into the cold tongue mixed layer and therefore a negligible rectification effect onto the cold tongue SST and contribution to the ENSO cycle (Shinoda et al. 2009; Wang et al. 2020). The real part of the TIW index (TIW1) is defined as the equally spaced and weighted (but with alternating signs) summation of SST anomalies at six red points along 0°–6°N as shown in Fig. 2a. To capture the westward propagation of TIWs, the imaginary part of the TIW index (TIW2) is defined in the same way, except the base points are all shifted by a fixed distance representing a 90° zonal phase shift as the black dots in Fig. 2b show:
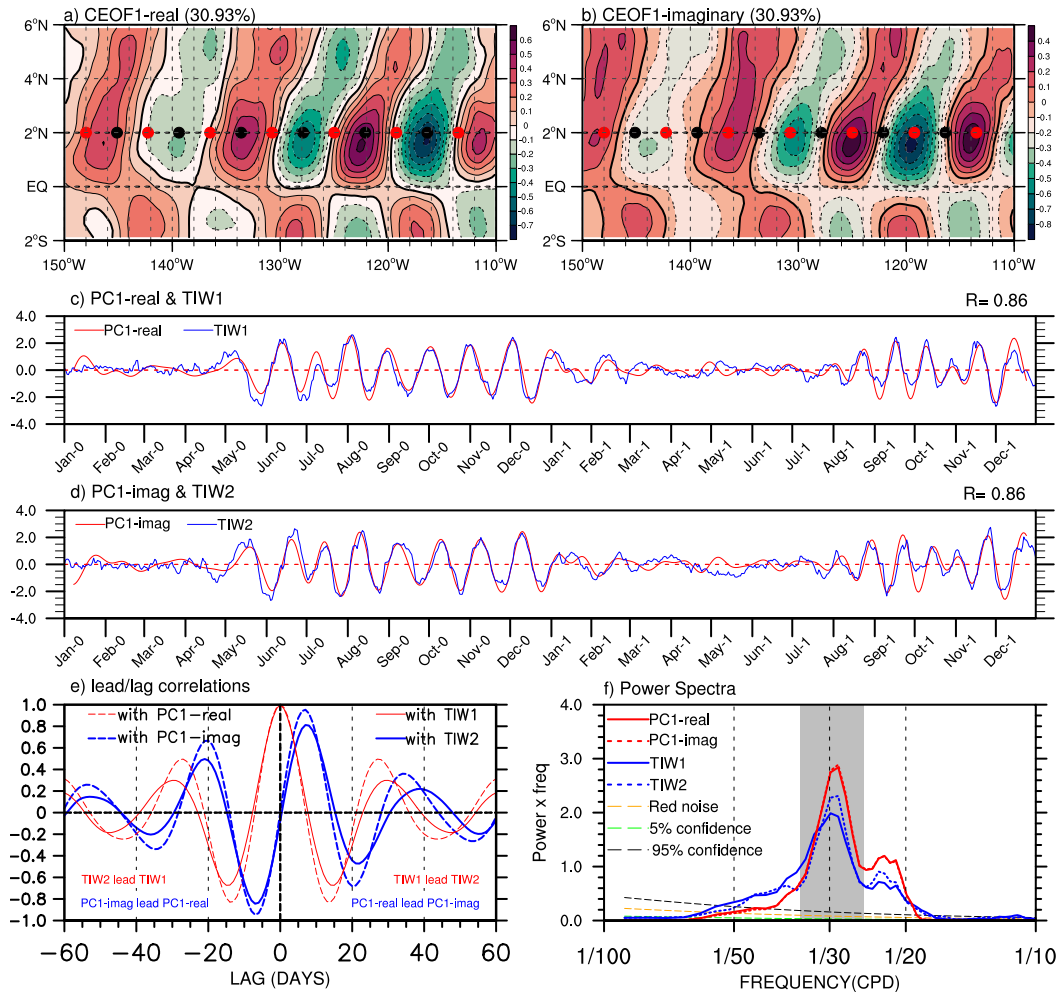
FIG. 2. (a),(b) Leading CEOF spatial patterns of SSTAs over the TIW active region (2°S–6°N, 110°–150°W) over the 2016–17 period [for the (a) real and (b) imaginary parts] obtained through a linear regression of SSTAs onto the normalized real part (PC1-real) and imaginary part (PC1-imag) of the leading PC time series. Red (black) dots show the positions of longitudinal nodes used to calculate TIW1 (TIW2). (c),(d) Corresponding normalized PC time series of leading CEOF mode (red lines) and complex TIW index (blue lines), respectively. Number 0 in parentheses denotes the year 2016, and the number 1 denotes the following year (2017). All results are statistically significant above the 99% confidence level. (e) Lead–lag correlations between TIW1 and TIW2 (solid blue line) and TIW1 autocorrelation (solid red line), and the same for the PCs (dashed lines and similar color code). (f) Power spectra of the normalized PC1 (red line) and TIW index time series (blue line); solid (dashed) lines are for the real (imaginary) part. The plotting format forces the area under the power curve to be equal to the variance in any frequency band. The gray bar indicates the approximate TIW frequency peak. The dashed orange line is the red-noise spectrum inferred from a first-order autoregressive process. The 5% (95%) confidence intervals are shown by the dashed green (black) lines.

$$\text{TIW1} = \Sigma \pm \text{SST}'(t, \text{nodes})/n,$$

$$\text{TIW2} = \Sigma \pm \text{SST}'\left(t, nodes + \frac{l}{4}\right)\bigg/ n,$$

$$Z = \text{TIW1} + i\,\text{TIW2},$$

where l represents the TIWs wavelength (in degrees), which is determined by the leading mode of the complex empirical orthogonal function (CEOF) (Fig. 2), and n is the number of points. The TIW amplitude is expressed as $|Z| = \sqrt{\text{TIW1}^2 + \text{TIW2}^2}$.

To prove the effectiveness of this simple index in capturing the TIWs signal, we perform a CEOF analysis (Barnett 1983; Boucharel et al. 2013; Xue et al. 2020) over the eastern equatorial Pacific (2°S–6°N, 150°–110°W) on the 10–60-day bandpass filtered daily SSTA from NOAA OISSTv2 during the 2016/17 La Niña period (Fig. 2). It should be noted that the results are not sensitive to the time period we choose. As a result, the first two leading modes account respectively for 30.93% and 23.82% of the total variance and are well separated from each other as per the criterion of North et al. (1982). Figures 2a and 2b show the

regression patterns of SSTA onto the real (PC1-real; red line in Fig. 2c) and imaginary (PC1-imag; red line in Fig. 2d) part, respectively, of the leading mode's principal component (PC1). They suggest a series of alternating cyclonic (wave trough) and anticyclonic (wave crest) circulations coupled with SSTAs north of equator. Relatively weak TIW patterns are also found south of equator. Two groups of fixed referenced points precisely have 90° zonal phase shift, which demonstrates the TIWs westward propagation similar to the CEOF phase pattern (not shown). In other words, TIW1 and TIW2, defined with these points, satisfy the orthogonal relationship, and allow us to capture the TIWs' propagating structures and characteristics. The PC1 time series (Figs. 2c,d) generally appear as a nearly quadrature pair and have high correlation with the complex TIW index previously defined ($R = 0.86$), again suggesting the good performance of the complex TIW index in capturing the TIW mode.

More evidence of the effectiveness of the complex TIW index in capturing TIW activity is provided in Figs. 2e and 2f. The lead–lag cross-correlations between TIW1 and TIW2 show that the maximum (minimum) positive (negative) correlation (~0.85) appears when TIW1 (TIW2) leads TIW2 (TIW1) by 5–10 days. The TIWs damping rate (nearly 1/23 day^{-1}) can be evaluated based on the TIW1 autocorrelation. PCs lead–lag correlations are similar to those calculated with TIWs indices. The power spectra also exhibit clear peaks corresponding to an intraseasonal periodicity at 20–50 days for all indices mainly capturing the ~33-day TIWs north of the equator (Fig. 2f). The fraction of total variance occurring in the 20–50-day range is ~0.9 for both TIWs (PCs) (not shown), which indicates that complex TIW index account for most of the variance of TIW activity and confirms that we can discard TIWs variability related to the Yanai mode (below 20 days). The results, which are highly consistent with previous studies (Boucharel and Jin 2020; Xue et al. 2020), reveal that the complex TIW index with a ~33-day period has a high consistency with the leading PC time series and could capture the overall TIWs characteristics accurately.

3. Contrasting evolutions of the 1998/99 and 2016/17 episodes

The evolution of the 1997–99 and 2015–17 El Niño/La Niña events is shown in Fig. 3a from observed ERSSTv5 data. The result shows that the 1997/98 El Niño began to develop around May 1997, reached its peak in November, and then subsequently weakened until it was officially declared to have ended in boreal spring 1998 and turned into a long-lasting and strong La Niña event. SSTAs followed a fairly similar developing phase during the 2015/16 El Niño on par with those of the 1997/98 event but experienced a significantly different decaying phase. SST anomalies decreased more rapidly and returned to zero in April. The most conspicuous contrast occurred during ENSO phase transition (May–June), and was possibly related to subsequent weaker and short-lived La Niña conditions as shown in Fig. 3b. In addition, the SSTA propagating pattern was also very different during this period, showing that positive SSTA propagated from the tropical eastern to western Pacific during 2016 while positive SSTA propagated eastward in 1998. The atmospheric responses, diagnosed by the 10-m wind

anomalies field from ERA5, were well coupled with the SSTA evolution for these two events (vectors in Figs. 3a,b). During the developing boreal spring and early summer of El Niño events, strong westerly anomalies appeared over the central-western Pacific near the date line. The wind anomalies then were shifted eastward to the central Pacific by around 20° of longitude when these two El Niño events entered their mature phases. However, remarkable differences in zonal wind anomalies in the central-western Pacific also occurred throughout their decaying phases. Unlike the 2015/16 event where the wind anomalies were fairly weak during the decaying phase, westerly wind anomalies during the 1997/98 El Niño turned rapidly into anomalous easterlies. The significant differences in the surface zonal wind anomalies evolutions motivate our detailed investigation of the possible mechanisms that could account for such different decaying processes.

Using the GODAS reanalysis product, we investigate the equatorial oceanic subsurface evolution for these two events in Figs. 3c and 3d. The thermocline evolution (indicated by the depth of the 20°C isotherm anomaly) was consistent with the recharge–discharge process transition from El Niño to La Niña (Jin 1997a). This is indicated by the eastward propagation of a strong downwelling Kelvin wave that transported warm water from the western to eastern Pacific during both El Niño developing phases followed by the eastward propagation of an upwelling Kelvin wave during La Niña developing phase (L'Heureux et al. 2017; Kakatkar et al. 2018). In general, strong discharge processes suggest the transitioning toward La Niña conditions, and indeed, a negative (i.e., deeper) equatorial 20°C thermocline depth (D20) anomaly emerged by March 2016, indicating a likely transition toward La Niña. However, this upwelling Kelvin wave appeared substantially weaker in 2016 than 1998 during the following boreal spring and summer. Consistently with previous study (Kakatkar et al. 2018), the evident contrast in equatorial wave dynamics with stronger (weaker) upwelling Kelvin waves during 1997/98 (2015/16) might contribute to the weaker La Niña conditions in 2016 than 1998. The weaker discharge process during 2015/16 El Niño is definitely a plausible candidate to explain the hindered development of the 2016 La Niña. However, the reasons for such a different discharge process between the two events are still unclear and so is the extent to which this mechanism is responsible for the weak 2016 La Niña event. Therefore, there is a strong incentive to investigate some other possible processes that may also explain the contrasted La Niña evolutions between these two events. In particular, considering the extremely strong TIW activity during the phase transition following the 2015/16 super El Niño event (Boucharel and Jin 2020), we hypothesize that oceanic-sourced TIWs could rectify into this linear discharge process through NDH. We investigate the role of TIW activity on La Niña phase transition in the next section.

4. Important role of TIW activity

a. Comparison of TIW activity between the two episodes

We first compare the TIW amplitudes between these two La Niña events using the complex TIW index defined in section 2
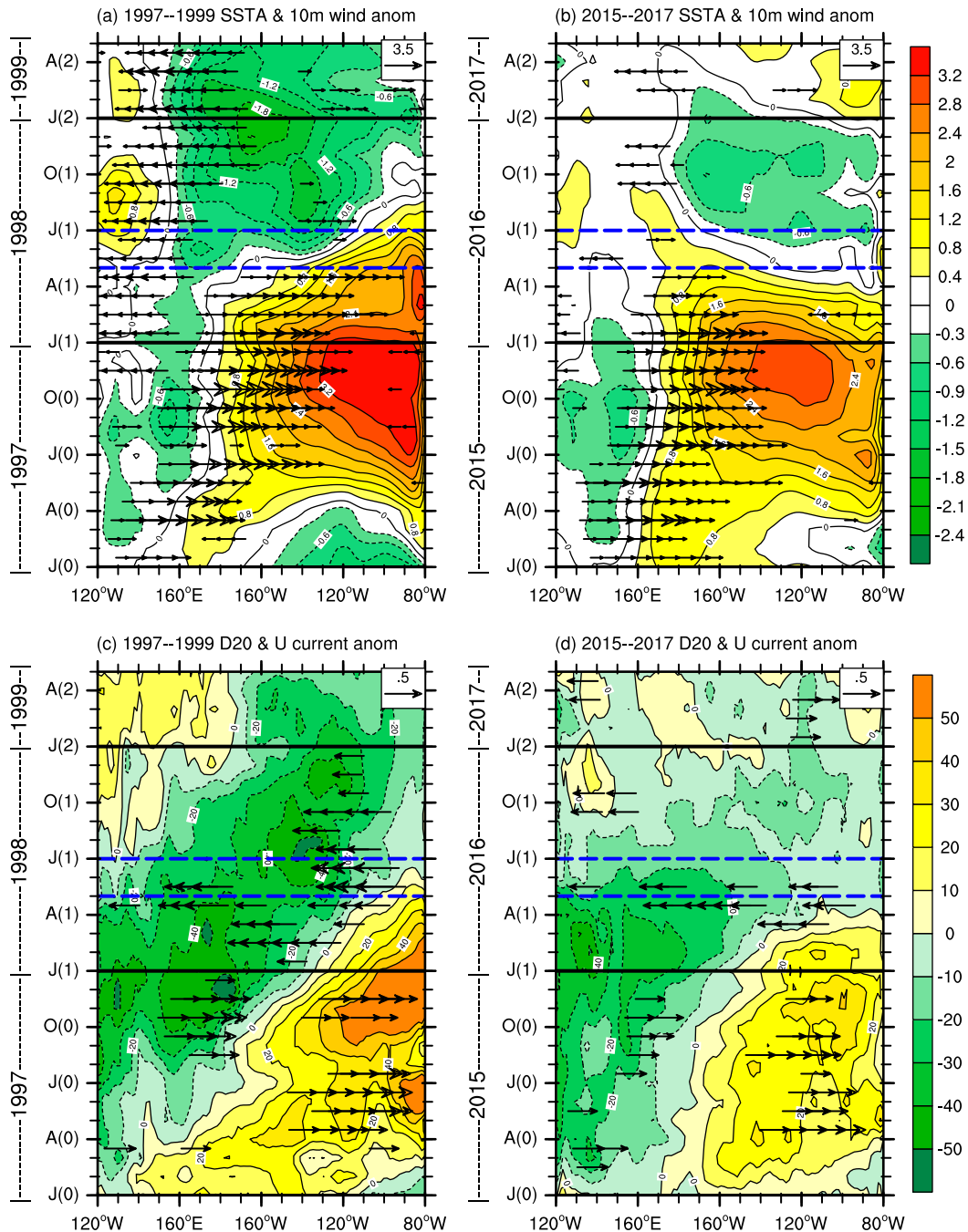
FIG. 3. The shading shows the evolution of equatorial SST anomalies (°C) and the vector fields show the anomalous 10-m zonal wind (m s⁻¹) averaged over 5°S–5°N for (a) the 1997/98 event and (b) the 2015/16 event. (c),(d) As in (a) and (b), but for the evolution of the equatorial 20°C thermocline depth (D20) anomalies and oceanic surface zonal current anomalies. The number 0 in parentheses denotes the ENSO developing year (1997 and 2015), the number 1 denotes the El Niño decaying year (1998 and 2016), and the number 2 denotes the following year (1999 and 2017). The legend at the upper-right corner of each panel indicates a reference vector magnitude.

from the NOAA product. As shown in Fig. 4a, the overall TIW amplitude during the boreal May–August of 2016 was much stronger than in 1998, and especially during the ENSO phase transition when TIW activity is the strongest (i.e., the early

boreal summer, May–June). Given that the seasonally varying TIWs tend to warm the equatorial cold tongue through meridional heat advection (Wang and McPhaden 1999), we hypothesize that TIW-induced heating could play an important

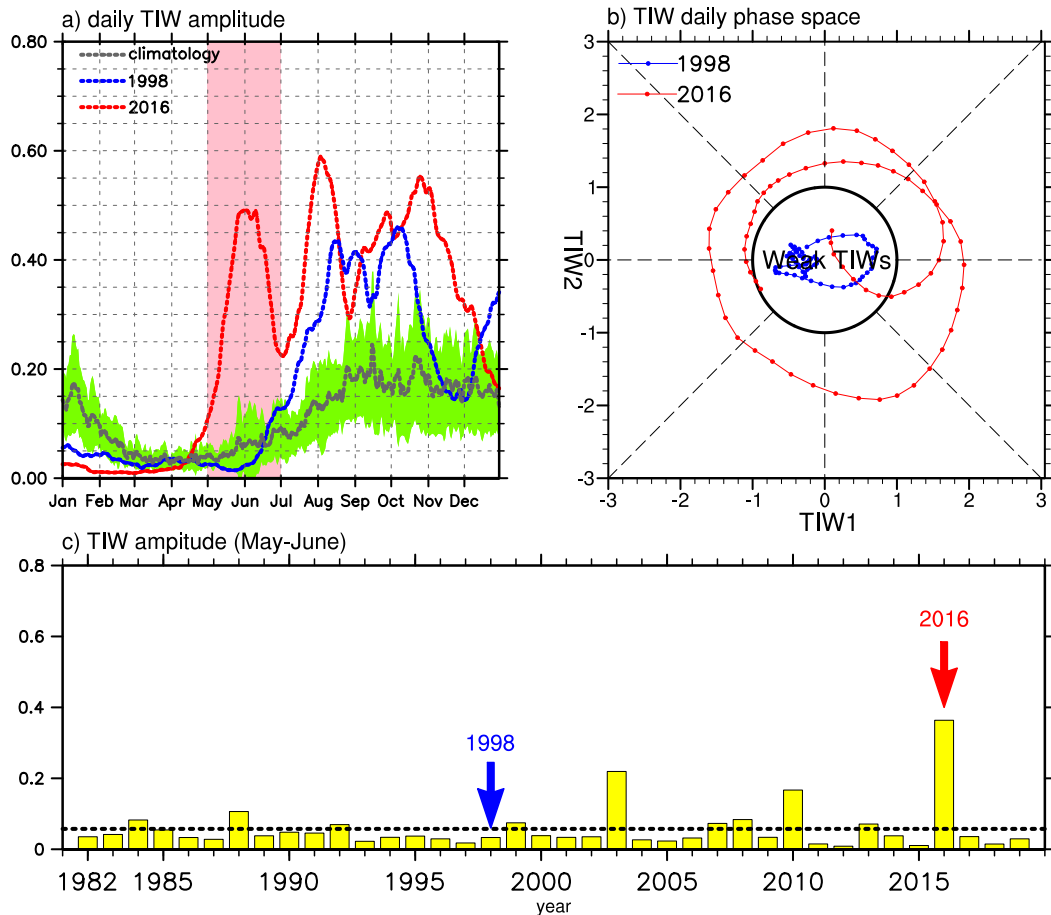FIG. 4. (a) Time series of the daily TIW amplitude for the 1998 (blue), the 2016 La Niña event (red), and the climatology (gray). The green shades represent one standard deviation error estimates. (b) (TIW1, TIW2) phase-space points for all available days during May–June for 1998 (blue) and 2016 (red). The region of weak TIW activity is labeled. (c) Annual TIW amplitude (May–June) during 1982–2018 (yellow bars) and the corresponding climatological mean state during ENSO phase transition (black dashed line).

role in hindering the 2016 La Niña development through mixing and entrainment of off-equatorial warm water into the eastern Pacific cold tongue. Considering the lead–lag behaviors of the TIW indices in Fig. 2e, we can diagnose the state of the TIW activity as a point in the two-dimensional phase space defined by TIW1 and TIW2, following the Madden–Julian oscillation phase-space diagram (Wheeler and Hendon 2004). This representation is shown for all days during the ENSO phase transition (May–June) in Fig. 4b. We observe oscillations characterized by a stronger TIW activity during the 2016 ENSO transition phase than during the 1998 transition. Additionally, while the TIW amplitude in the boreal spring of 1998 was very weak (i.e., below the climatological mean state), the 2016 TIWs were the most active during that season compared with the previous four decades (Fig. 4c). This represents an undeniable motivation to explore further the potential role of TIWs on the ENSO phase transition.

Furthermore, we also investigate the spatial pattern of the TIW activity based on another commonly used TIW definition, measured by the standard deviation (variance) of bandpass

filtered SSTA from NOAA at the TIW time scale (10–60 days) (e.g., Yu and Liu 2003; Wu and Bowman 2007; Im et al. 2012). Figure 5 shows the two Hovmöller diagrams (averaged over 0°–6°N) of the TIW-related SST standard deviation during the 1998 and 2016 events and their difference. TIW activity was suppressed during the winter–spring SST peak of both events and then became more active than normal when the equatorial Pacific SSTAs were characterized by La Niña conditions. In comparison, TIWs started to develop and propagate westward rapidly since the early spring in 2016 and persisted until the peak of La Niña (end of the calendar year) (Fig. 5b), whereas TIW activity was only apparent in the cold tongue from July in 1998 when the La Niña–related SSTA prevailed in the eastern Pacific (Fig. 5a). Overall, the TIW activity was most notably different between these two events during the ENSO phase transition (i.e., May–June) (Fig. 5c). These results are consistent with those estimated from our TIW definition as shown in Fig. 4. Note that our TIW definition inferred from the complex index does not require any filtering, suggesting that it is a more straightforward way to capture TIW characteristics.
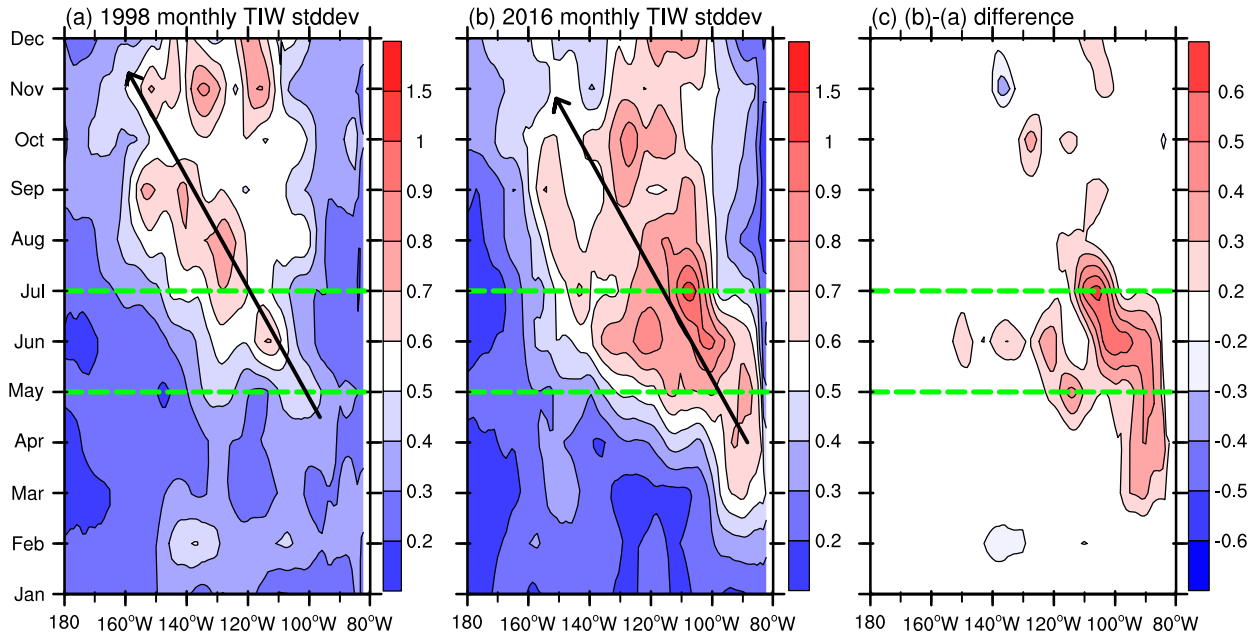
FIG. 5. Longitude–time diagrams of monthly TIW standard deviations averaged over 0°–6°N for (a) 1998 and (b) 2016, and (c) their difference.

b. TIW-induced nonlinear oceanic heat flux

It has been highlighted that the contribution of TIWs onto ENSO could be estimated from the rectified effect of anomalous temperature transport by anomalous currents at intraseasonal scale, which is referred to as oceanic eddy heat flux (e.g., Baturin and Niiler 1997; Menkes et al. 2006; Jochum and Murtugudde 2006; Jochum et al. 2007; Xue et al. 2020). As the divergence of the eddy heat flux, TIW-induced NDH is a dynamical heating source for ocean temperatures, which could be referred to as the direct TIWs' rectification effect onto the ENSO heat budget. Thus, we hypothesize here that TIW-induced NDH may have played an important role as a warming advection term and may have contributed to the early weakening of the 2016/17 La Niña. To understand the important role of TIW activity on the ENSO phase transition, we quantify the TIW-induced oceanic eddy heat flux and NDH within the mixed layer from the GODAS product. Classically, each variable X can be separated into a mean climate state (overbar), low-frequency component (tilde) (over 60 days), and an eddy component (prime) and thus can be expressed as $X = \overline{X} + \tilde{X} + X'$. As TIWs have a broad spectral peak in the 10–60-day range, we can evaluate the effect of TIWs in seasonal mean as follows:

$$\mathbf{HF}_{\text{TIW}} = \langle -\mathbf{V}'\mathbf{T}' \rangle = \langle -u'T' \rangle \mathbf{i} + \langle -v'T' \rangle \mathbf{j} + \langle -w'T' \rangle \mathbf{k},$$

$$\text{NDH}_{\text{TIW}} = \nabla \cdot \mathbf{HF}_{\text{TIW}} = \left\langle -\frac{\partial u'T'}{\partial x} \right\rangle + \left\langle -\frac{\partial v'T'}{\partial y} \right\rangle + \left\langle -\frac{\partial w'T'}{\partial z} \right\rangle,$$
(1)

where T' and (u', v', w') represent the oceanic mixed-layer anomalies of temperature and ocean currents at the TIW time scales. $\mathbf{HF}_{\text{TIW}}$ and NDH_{TIW} represent the TIW-induced oceanic

heat flux and NDH, respectively. The bracket denotes a 3-month running mean. The horizontal advections are averaged within the top 50 m, which roughly represents the mixed layer depth. Previous studies have shown that the TIW-induced zonal and vertical heat flux components onto the mean climate state and ENSO variability are negligible within the mixed layer (Hansen and Paul 1984; Bryden and Brady 1989; Menkes et al. 2006; Xue et al. 2020), which is consistent with our analysis (not shown). Therefore, the TIW-induced heat flux ($\mathbf{HF}_{\text{TIW}}$) and associated NDH (NDH_{TIW}) within the mixed layer could be largely represented by the meridional components ($-v'T'$) and ($-\partial v'T'/\partial y$), respectively. Figure 6a shows the meridional TIW-induced heat flux regressed onto the monthly TIW amplitude from GODAS. The TIW amplitude, proportional to T'^2, shows a highly positive correlation with the TIW-induced heat flux, suggesting that meridional eddy current anomalies (v') has a strong spatial coherence with the eddy temperature anomalies (T') and therefore a strong meridional convergence of equatorward heat flux. TIW activity can then produce equatorward heat flux from the northern off-equatorial Pacific region into the cold tongue by mixing the warm and cold water across the SST front. This is confirmed by the zonally averaged summertime meridional eddy heat transport (cf. Fig. 6b) that displayed a much larger southward heat transport from north of the equator (0°–6°N) in 2016 than in 1998. Similarly, a northward transport can also be detected south of the equator (2°S–0°) but with a much weaker amplitude (Fig. 6b), consistent with TIWs being weaker on the southern side of the cold tongue front. This heat flux convergence, consistent with the estimation in observations by Bryden and Brady (1989) and Baturin and Niiler (1997), represents a significant
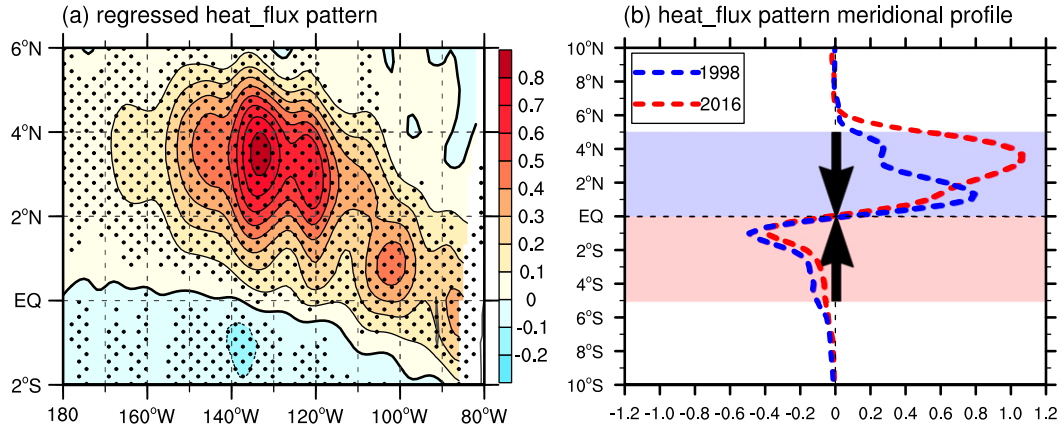
FIG. 6. (a) TIW-induced meridional heat flux regressed onto the standardized monthly TIW amplitude for all months during 1980–2018. Values exceeding the 99% confidence level are marked by black dots. (b) The blue line and red line denote the meridional structures of zonal mean (110°–150°W) heat flux pattern (units: 10^5 m °C^{-1} month^{-1}) during ENSO phase transition (May–June) for 1998 and 2016, respectively. The black arrows indicate the eddy heat flux convergence.

contribution to the equatorial SST warming during the ENSO phase transition, especially in 2016.

c. Heat budget during ENSO phase transition over the TIW region

Figure 7 displays the three-dimensional mixed-layer heat budget during the El Niño–La Niña phase transition over the most active TIW region (5°S–5°N, 110°–150°W) for the 1998 and 2016 events. Since the seasonal averaged TIW contributions to the ENSO budget from the cross mean-eddy terms $-[\tilde{u}(\partial T'/\partial x) + \tilde{v}(\partial T'/\partial y) + \tilde{w}(\partial T'/\partial z)]$ and $-[u'(\partial \tilde{T}/\partial x) + v'(\partial \tilde{T}/\partial y) + w'(\partial \tilde{T}/\partial z)]$ vanish, the ENSO mixed-layer heat budget could be simplified as follows:

$$\frac{\partial \tilde{T}}{\partial t} = -\left(\tilde{u}\frac{\partial \overline{T}}{\partial x} + \tilde{v}\frac{\partial \overline{T}}{\partial y} + \tilde{w}\frac{\partial \overline{T}}{\partial z}\right) - \left(\overline{u}\frac{\partial \tilde{T}}{\partial x} + \overline{v}\frac{\partial \tilde{T}}{\partial y} + \overline{w}\frac{\partial \tilde{T}}{\partial z}\right)$$
$$- \underbrace{\left(\tilde{u}\frac{\partial \tilde{T}}{\partial x} + \tilde{v}\frac{\partial \tilde{T}}{\partial y} + \tilde{w}\frac{\partial \tilde{T}}{\partial z}\right)}_{\text{NDH}} + \tilde{Q} + \widehat{\text{NDH}_{\text{TIW}}}. \quad (2)$$

The terms, from left to right, represent the mixed layer temperature tendency ($\partial \tilde{T}/\partial t$), the anomalous zonal and meridional advection terms [$-\tilde{u}(\partial \overline{T}/\partial x)$ and $-\tilde{v}(\partial \overline{T}/\partial y)$], anomalous upwelling advection term [$-\tilde{w}(\partial \overline{T}/\partial z)$], mean horizontal advection terms [$-\overline{u}(\partial \tilde{T}/\partial x)$ and $-\overline{v}(\partial \tilde{T}/\partial y)$], the mean upwelling advection term [$-\overline{w}(\partial \tilde{T}/\partial z)$], low-order NDH associated with
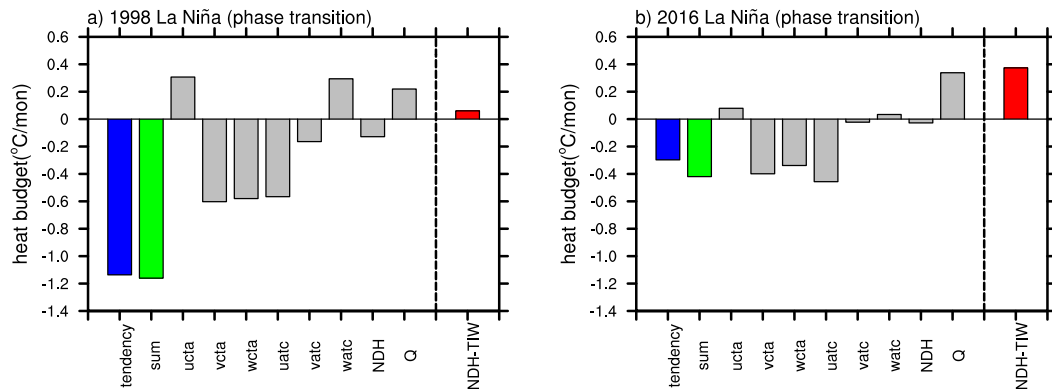
FIG. 7. Comparison of the mixed layer SST heat budget analysis over the TIW active region (5°S–5°N, 110°–150°W) (units: °C month^{-1}) during the ENSO phase transition (May–June) of (a) 1998 and (b) 2016. Here ''sum'' (green bar) means the summation of all terms on the right side of Eq. (4). The bars, from left to right, indicate the mixed layer temperature tendency, sum of all terms on the right-hand side of Eq. (4), the anomalous zonal and meridional advection terms [$-\tilde{u}(\partial \overline{T}/\partial x)$ and $-\tilde{v}(\partial \overline{T}/\partial y)$], anomalous upwelling advection term [$-\tilde{w}(\partial \overline{T}/\partial z)$], mean horizontal advection terms [$-\overline{u}(\partial \tilde{T}/\partial x)$ and $-\overline{v}(\partial \tilde{T}/\partial y)$], mean upwelling advection term [$-\overline{w}(\partial \tilde{T}/\partial z)$], low-order NDH associated with the low-frequency (>60 days) variability [$\tilde{u}(\partial \tilde{T}/\partial x) + \tilde{v}(\partial \tilde{T}/\partial y) + \tilde{w}(\partial \tilde{T}/\partial z)$], the atmospheric heat flux (Q), and TIW-induced NDH (NDH$_{\text{TIW}}$).

the low frequency (>60 days) variability, the atmospheric heat flux (Q), and TIW-induced NDH (NDH$_{TIW}$). Previous studies have demonstrated that TIW-induced heat flux convergence (NDH$_{TIW}$) is basically proportional to TIW amplitude (i.e., NDH$_{TIW} \propto |Z|^2$) (Boucharel and Jin 2020; Xue et al. 2020). Based on the eddy heat flux, the TIW-induced NDH can be simply quantified as the following approximate estimation derived in Xue et al. (2020):

$$
\begin{aligned}
\mathrm{NDH_{TIW}} &= -\frac{\partial \langle v'T' \rangle}{\partial y} = -\frac{\Delta \langle v'T' \rangle}{L} = -\frac{\langle v'T' \rangle_{0°-5°N} - \langle v'T' \rangle_{5°S-0°}}{L} \\
&= \frac{\sigma}{L} \times \left\langle |Z|^2 \right\rangle + \varepsilon,
\end{aligned}
\tag{3}
$$

where σ represents a scaling factor obtained as the regression coefficient of the TIW-induced heat flux onto the TIW variance; $|Z|^2$ represents the TIW variance in observation from NOAA OISSTv2; L is the meridional effective scale of TIWs and reflects the width of the spatial region used to average these quantities; and ε is a constant term. This simplified approach could avoid the interference from the equatorial intraseasonal Kelvin waves and reduce the computational bias due to the inaccuracy of TIW intensity in GODAS.

As shown in Fig. 7, during the ENSO phase transition, the mixed layer temperature tendency for the 1998 and 2016 La Niña events was approximately $-1.20°$ and $-0.33°$C month^{-1}, respectively, characterizing very different La Niña growth rates. The sum of linear dynamical terms both made positive contributions to the negative temperature tendency for the 1998 and 2016 La Niña (not shown). From the Fig. 7, the major contributors of positive dynamical feedbacks were the anomalous zonal advection term $[-\tilde{u}(\partial \overline{T}/\partial x)]$, mean meridional advection term $[-\overline{v}(\partial \tilde{T}/\partial y)]$, and mean upwelling advection term $[-\overline{w}(\partial \tilde{T}/\partial z)]$. As shown in Figs. 3c and 3d, the pronounced eastward zonal current anomalies ($\tilde{u} < 0$) as a response to wind forcing during this period have cooled the SST in the eastern Pacific through upwelling Kelvin waves. The negative thermocline depth anomalies and the negative temperature anomalies in the equatorial Pacific also strengthened the surface cooling through the climatological meridional overturning circulation and mean upwelling. These distinctive positive feedback processes contributed to the distinct La Niña behaviors between these two events. We have also examined the contribution of low-order NDH at low frequency (over 60 days) to the La Niña phase transition, which turned out to be weak for both events. Finally, the differences in the atmospheric heat fluxes between these two events remain small. This confirms that the contribution of TIW-induced NDH, shown to warm the cold tongue with a rate of 0.37°C month^{-1} in 2016 and 0.05°C month^{-1} in 1998, could explain the observed differences between the two events. In 2016, the considerable magnitude of the TIW-induced NDH was nearly comparable to those from the usual contributors to the ENSO growth rate, namely the atmospheric heat fluxes, the zonal advection, thermocline, and Ekman feedbacks (Wang and McPhaden 1999; Boucharel et al. 2015). In subsequent seasons, TIW-induced NDH showed comparable magnitudes for both events (not shown) since the TIWs were both active in the fall as shown in Fig. 4a. The results suggest that persisting TIW-induced heat flux and NDH can also explained to some extent the diversity of the subsequent La Niña development.

5. Possible mechanisms for the strong TIW activity in 2016

Although the eastern Pacific was characterized by weak La Niña conditions during both the 1998 and 2016 at the early stage of the ENSO phase transition (Fig. 1a), the development of the 2016 event came to a halt when the strong TIW activity kicked in and prevented further cooling of the cold tongue. This raises the question: why was the TIW activity much stronger in 2016 when the equatorial SSTAs were in fact fairly similar? Previous studies show that TIWs could arise from the barotropic instabilities (e.g., Cox 1980; Philander 1976), baroclinic instabilities (e.g., Hansen and Paul 1984; Wilson and Leetmaa 1988; Yu et al. 1995), and Kelvin-Helmholtz mechanism (Proehl 1996). To investigate the possible mechanisms responsible for the different TIW activity between the 1998 and 2016 ENSO phase transition, we estimate such instabilities from an eddy kinetic energy (EKE) budget derived from the momentum equations (Qiao and Weisberg 1995). The time-mean EKE [EKE $= \rho_0(\overline{u'^2 + v'^2})/2$] equation is given by

$$
\begin{aligned}
(\mathrm{EKE})_t - \overline{v} \cdot \nabla(\mathrm{EKE}) - \overline{v' \cdot \nabla(\mathrm{EKE})} &= \overline{v' \cdot \nabla P'} + \mathrm{BTR} + \mathrm{BCR} + \mathrm{KH} - \varepsilon, \\
\mathrm{BTR} &= -\rho_0 [\overline{u'u'}\overline{u}_x + \overline{u'v'}(\overline{u}_y + \overline{v}_x) + \overline{v'v'}\overline{v}_y], \\
\mathrm{BCR} &= -\overline{\rho'gw'}, \\
\mathrm{KH} &= -\rho_0(\overline{u'w'}\overline{u}_z + \overline{v'w'}\overline{v}_z),
\end{aligned}
\tag{4}
$$

where the overbars denote the 3-month running mean and primes denote the TIW component (10–60 days), $\mathbf{v}$ is the velocity vector, P is the pressure, ρ_0 is the density of ocean water, g is the acceleration of gravity, and ε is the dissipation of EKE. The first term on the right-hand side of the EKE equation represents the contribution to the redistribution of eddy energy by the pressure work. BTR represents the barotropic energy conversion between the mean and eddy flows, which could gain energy from mean kinetic energy. BCR denotes the baroclinic energy conversion between kinetic energy and the available potential energy of eddy flows. KH represents the Kelvin–Helmholtz energy conversion due to the vertical shear of currents. Since the advection and pressure work terms in Eq. (4) could only contribute to redistributing the EKE (Im et al. 2012), we focus on the relative contributions of mechanic production terms BTR, BCR, and KH.

Previous studies showed that localized energy budget might be misleading to assess the energy sources and sinks of TIWs
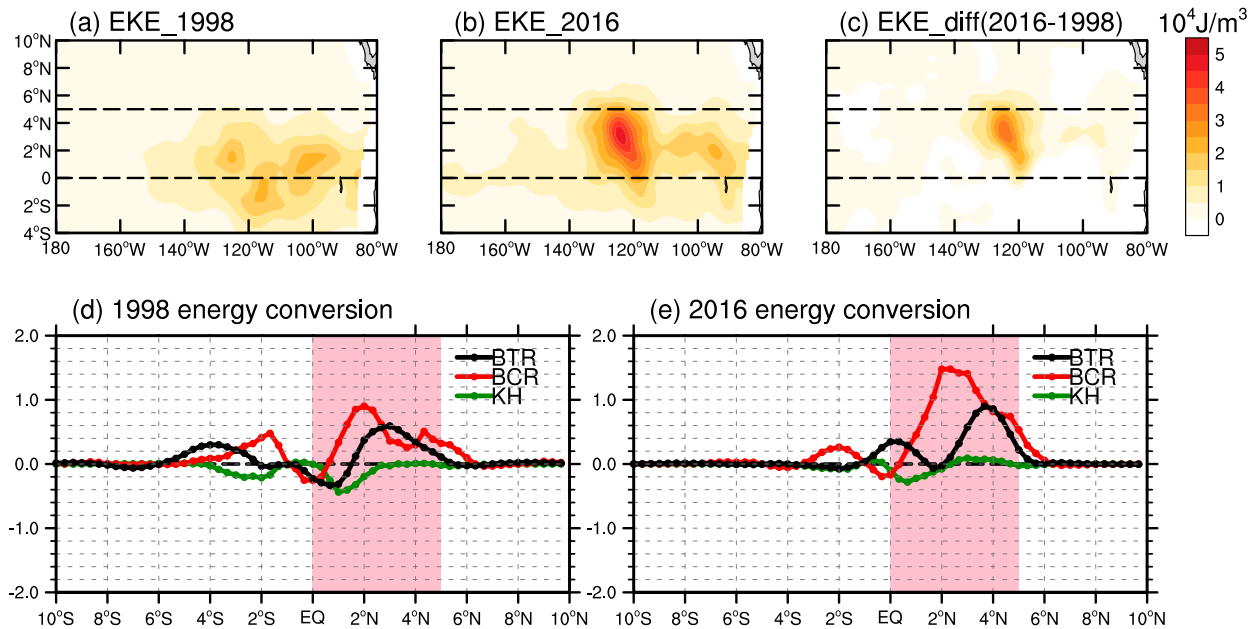
FIG. 8. Maps of mean TIW EKE (units: 10^4 J m^{-3}) over the TIW region (4°S–10°N, 180°–80°W) during the ENSO phase transition of (a) 1998 and (b) 2016, and (c) their difference. (d),(e) Zonally averaged energy conversion (units: 10^5 W m^{-3}) over the Niño-3 region (90°–150°W) between EKE and the mean kinetic energy (black dotted line), available potential energy (red dotted line), and Kelvin–Helmholtz energy conversion (green dotted line) for 1998 and 2016, respectively.

because of the propagation of energy (Masina et al. 1999; Masina and Philander 1999). Thus, we apply a time average (May–June) for the energy analyses over the Niño-3 region (5°S–5°N, 110°–170°W), which is representative of the steady energy conversion. Figures 8a–c show the time and mixed layer (0–50 m) average of EKE spatial patterns during the 1998 and 2016 ENSO phase transition (May–June) along with their difference. As shown in Figs. 8a and 8b, EKE shows a meridionally asymmetric distribution and was mostly confined to the north of the equator over the TIW active region, particularly in 2016. The mean EKE associated with TIWs was much stronger in 2016 than that in 1998 (Fig. 8c). We now investigate the respective contributions of the dominant instability mechanisms, BTR, BCR, and KH to the time-mean (May–June) EKE budget.

Both the 1998 and 2016 events show positive BTR with comparable amplitudes and therefore similar kinetic energy conversion from the mean flow to the TIWs during the phase transition (Figs. 8d,e). In comparison, the baroclinic energy conversion (BCR) was much larger in May–June of 2016 than in 1998, indicating a much stronger baroclinic instability in 2016. KH always had small and negative values mainly over the region of 0°–2°N, suggesting that TIWs transfer the Kelvin-Helmholtz energy back to the mean state, which is unfavorable to the TIW-related eddy persistence. While the barotropic and baroclinic instability terms were comparable during 1998, suggesting that both instabilities contributed to the associated TIW activity, the baroclinic energy conversion was evidently the dominant mechanism for the TIWs' growth and persistence during the phase transition of the 2016 La Niña event.

Early studies found that the baroclinic energy conversion from available potential energy to eddy kinetic energy is directly linked to the meridional SST gradient along the SST front immediately north of the equator (e.g., Masina et al. 1999; Yu and Liu 2003; Xue et al. 2020). During the 2016 ENSO phase transition, the subtropical North Pacific was marked by significant positive SST anomalies (Fig. 9b) that leaded to a substantial increase of the meridional SST gradient over most of the TIW active region (Fig. 9c). In contrast, such subtropical SST anomalies were nonexistent in 1998, and despite cooler anomalies along the equator the related meridional SST gradient was relatively weak (Fig. 9a). This suggests that the positive SSTAs in the northeastern off-equatorial Pacific were responsible for the strong baroclinic instability and associated TIW activity during the 2016 ENSO phase transition, which in turn hindered the development of the subsequent La Niña through enhanced advection of warm water into the cold tongue.

To emphasize the relationships between year-to-year SST conditions in the eastern equatorial Pacific and TIW activity, Fig. 10a shows a scatterplot between the Niño-3.4 index and interannual TIW-induced NDH during ENSO phase transition (May–June). This relationship exhibits a nonlinear behavior indicating that the TIW-induced NDH is modulated by ENSO and acts as asymmetric negative feedback onto ENSO (Boucharel and Jin 2020; Xue et al. 2020). However, the relationship exhibits some discrepancies. In particular, it breaks down for the 2016 La Niña event, as a considerable TIW-induced NDH accompanies a weak Niño-3.4 index. This is because Niño-3.4 index is not sufficient to depict the meridional SST gradient in this region and grasp the
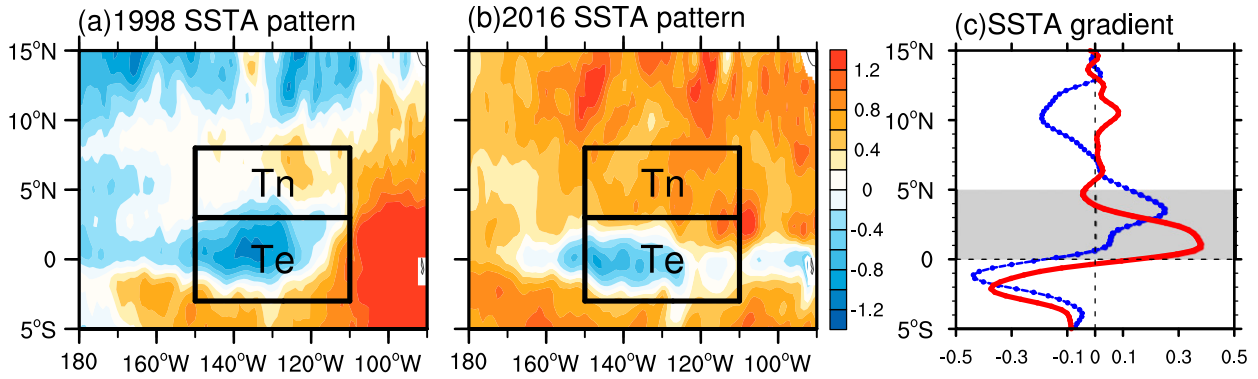
FIG. 9. Sea surface temperature anomalies (SSTA) (units: °C) during ENSO phase transition (May–June) in (a) 1998 and (b) 2016. (c) Meridional SSTA gradient (units: 10^5 °C m^{-1}) profile averaged over zonal TIW active region (110°–150°W) for 1998 (blue dotted line) and 2016 (red dotted line).

baroclinic instability. To better delineate the dependence of the interannual modulation of TIWs growth rate on the baroclinic instability, we define a new index (NiñoD; Xue et al. 2020) instead of the Niño-3.4 index as the meridional SST difference between the subtropical northeastern Pacific (Tn: 3°N–8°N, 150°–110°W) and the eastern equatorial Pacific (Te: 3°S–3°N, 150°–110°W), which are labeled in Figs. 9a and 9b. The nonlinear relationship between the NiñoD index and TIW-induced NDH is shown in Fig. 10b. The NiñoD index, which better accounts for the baroclinic instability than the Niño-3.4 index, exhibits a stronger relationship with the TIW-induced NDH, consistently with previous study (Xue et al. 2020). This indicates that SSTAs in the northeastern off equatorial Pacific could be treated as an independent precursor of ENSO phase transition through their modulating effect on the baroclinic instability and TIWs growth rate.

The underlying physical mechanism responsible for the strong SSTAs in this northern region remains unclear. Some studies argued that they are possibly related to the extratropical background state, in particular associated with the Pacific decadal oscillation (PDO) (Su et al. 2018), Pacific meridional mode (PMM) (e.g., Vimont et al. 2001, 2003a,b; Chiang and Vimont 2004), and the marine heat wave (the so-called Blob phenomenon) (Wu et al. 2018). Here, we argue that the positive SSTAs could be attributed to the long-lasting ENSO discharge processes since 2015/16 El Niño was regarded
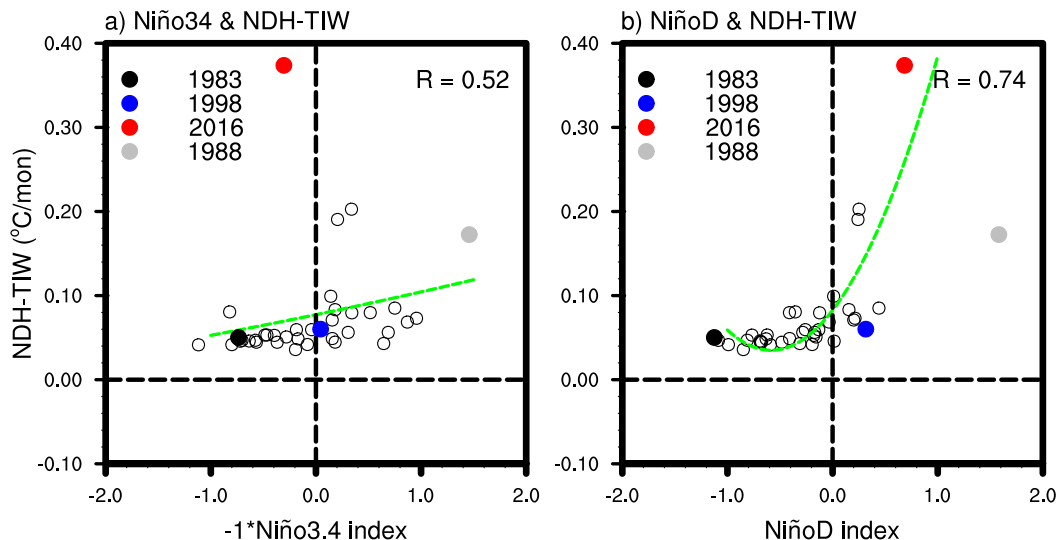

FIG. 10. Scatterplots of the relationship of the monthly mean (a) Niño-3.4 index and (b) NiñoD index, respectively, with the reconstructed TIW-induced NDH during the ENSO transition phase (May–June) from 1982 to 2018. The green lines indicate the nonlinear regression lines and the nonlinear correlation coefficients (R) are labeled in the upper-right corner of the corresponding panel.
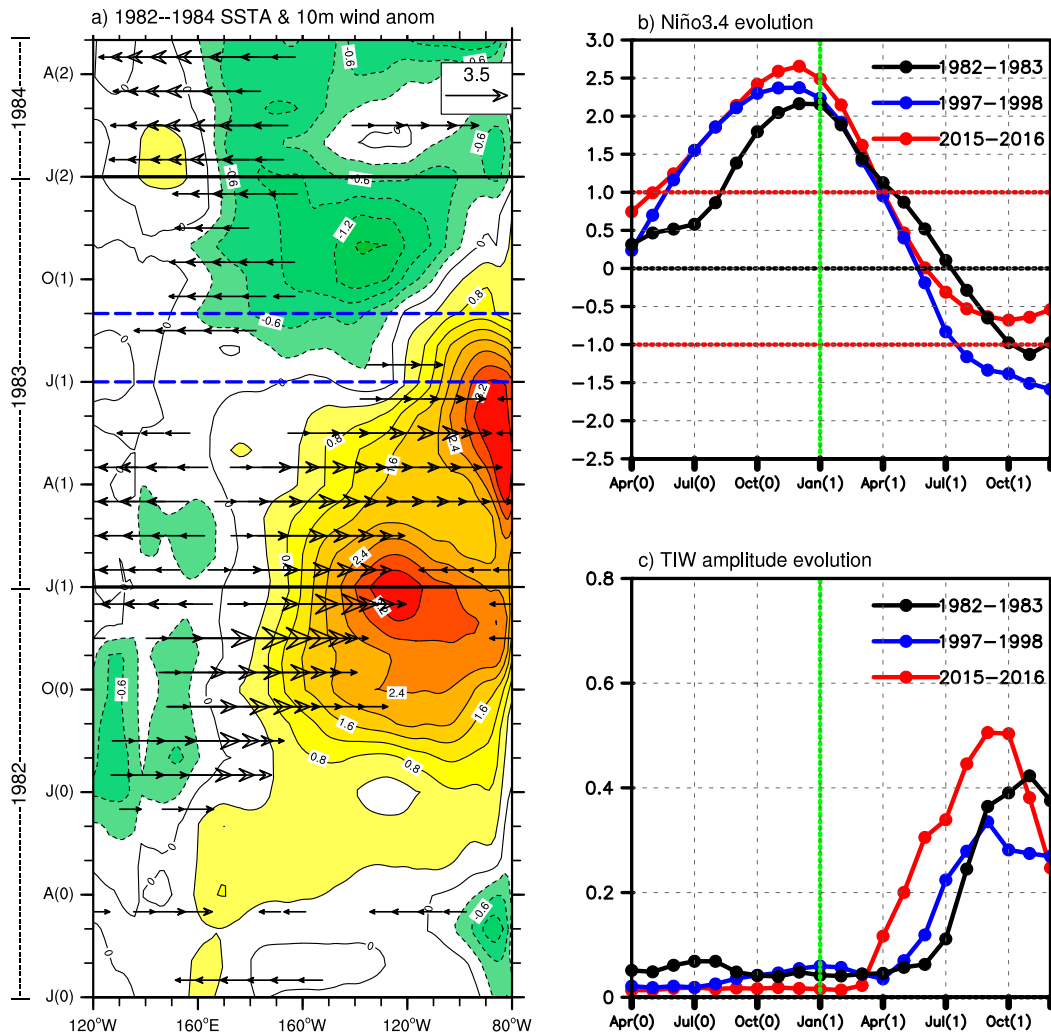
FIG. 11. Schematic diagram illustrating the dynamical mechanism responsible for hindering the 2016 La Niña development through the equatorward heat transport from the strong TIW activity.

as a protracted event that first appeared early in 2014 and matured in 2015. However, this issue is beyond the scope of this paper and requires to be further addressed in the future.

6. Summary and discussion

By most measures, the 2015/16 El Niño was one of the strongest on record, on par with the 1997/98 super El Niño event. However, the growth rates of the subsequent La Niña events differed significantly especially during their phase transition (May–June). Remarkably cold SSTAs appeared in the equatorial Pacific during the 1997/98 La Niña event, while the 2016/17 La Niña turned out to be a weak and short-lived event. We demonstrate in this study that the extremely strong TIW activity in the early boreal summer of 2016 played an important role in hindering the subsequent La Niña development. The main physical processes are summarized in the schematic diagram (Fig. 11).

Pronounced differences in off-equatorial conditions were found in the subtropical northeastern Pacific, which was marked by strong positive SSTAs during the post-2016 phase transition, whereas nearly neutral conditions occurred in this phase following the 1997 event. These positive SSTAs increased the meridional SST gradient across the SST front in 2016, thereby strengthening the baroclinic instability and favoring an enhanced TIW activity through baroclinic energy conversion. This extremely strong TIW activity could transport off-equatorial heat into the cold tongue through mixing and entrainment (section 5). We quantify the TIWs contribution onto ENSO through the high-frequency (i.e., TIW time scales) nonlinear rectification processes from the temperature advection. The TIW-induced NDH contributed to around 0.4°C warming per month during the early summer (May–June) following the peak of the 2015/16 El Niño and was shown to be an undeniably important factor inhibiting the 2016 La Niña development (section 4). The results here suggest that further investigation of the influence of oceanic-sourced TIWs and their deterministic interaction with ENSO onto ENSO diversity and complexity could ultimately lead to improved ENSO

performance in GCMs and prediction skills of seasonal climate forecast systems.

This raises the question of TIWs influence on the other compelling extreme ENSO event, the 1983/84 La Niña following the 1982/83 "super El Niño." This La Niña was considered a weak event as SSTA in the Niño-3.4 region barely reached −1.0°C at the peak of the event. Compared to the other two La Niña events investigated in the present study (1998/99 and 2016/17), this event was characterized by a delayed phase transition (July–September) as the El Niño signal persisted long after the classic boreal winter maturity with still large positive SSTAs in May and June 1983 (Figs. 12a,b). Therefore, the weak TIW amplitude due to weak meridional SST gradient during this period (May–June) could not contribute to the 1983 La Niña development (Figs. 4c and 12c). However, during 1983's delayed ENSO phase transition (July–September), TIW amplitude was similar to that in 2016, which suggests that this delayed TIW activity may also played an important role in hindering the 1983 La Niña development through a similar mechanism to the one described in this paper. Although there is an overall seasonal synchronization of ENSO phase transition, ENSO diversity requires careful assessment of each event's individual time evolution. Indeed, when adjusting this transition time, the contribution of TIWs onto ENSO could also be detected in some other events especially for strong La Niña events, although the associated strong TIW activity being modulated by La Niña conditions somehow blurs the causality of this mechanism. However, this suggests that TIW activity may act as a significant negative feedback onto ENSO development, a subject beyond the scope of this paper but certainly worthy of future investigations.

Although our analysis puts forward TIWs as a plausible mechanism that hindered the 2016 La Niña development, other mechanisms, described in the introduction, might also have played a role, possibly equally as important, during this peculiar ENSO event. In particular, the weak discharge process during the 2015 El Niño could be a primary factor responsible for the weakening of 2016 La Niña, whereas the large discharge process during 1997 El Niño leads to the following strong La

FIG. 12. (a) The shading shows the evolution of equatorial SST anomalies (°C) and the vector field shows the anomalous 10-m zonal wind (m s^{-1}) averaged over 5°S–5°N for the 1982/83 event. (b) Time evolution of SST anomalies for the El Niño/La Niña events of 1982/83 (black), 1997/98 (blue), and 2015/16 (red) in the Niño-3.4 region (5°N–5°S, 120°–170°W). (c) Time evolution of TIW amplitude of 1982/83 (black), 1997/98 (blue) and 2015/16 (red).

Niña (e.g., Kakatkar et al. 2018). As shown in Fig. 13a, the weak-discharged western equatorial Pacific oceanic heat content (WWVw) in boreal fall is the best ENSO predictor beyond 1 year ($R = 0.47$), especially for strong La Niña events (Planton et al. 2018). We can observe the stronger negative WWVw related to a stronger discharge process during the 1997 El Niño than during 2015, which contributed to the strong subsequent 1998 La Niña development. Furthermore, the PMM might also have prevented the strong discharge process through the counteracting TWC (e.g., Anderson et al. 2013; Amaya 2019; Chakravorty et al. 2020). In Fig. 13b, PMM during May and June has indeed a high correlation with the following equatorial SSTA condition at the mature phase (November–January). This suggests that the strong 2016 PMM event, which characteristically features positive SSTAs in the northern subtropical Pacific, could

have hindered the 2016 La Niña development through the associated TWC mechanism. In addition, the long-lasting WWEs associated with atmospheric intraseasonal variability could also influence ENSO and have played a role in the 2016 phase transition by the transport of warm water through downwelling Kelvin waves (e.g., Seiki and Takayabu 2007; Chen et al. 2015; Hu and Fedorov 2016, 2019). Finally, TIW–Kelvin wave interactions also may have contributed to hinder the 2016 La Niña development (Holmes and Thomas 2016).

With all of these factors that contribute to the ENSO diversity and complexity observed in recent decades (Timmermann et al. 2018), a more comprehensive and precise investigation of the respective influence of tropical versus subtropical factors and internal nonlinear processes versus external forcing on ENSO evolution and in particular its phase transition is
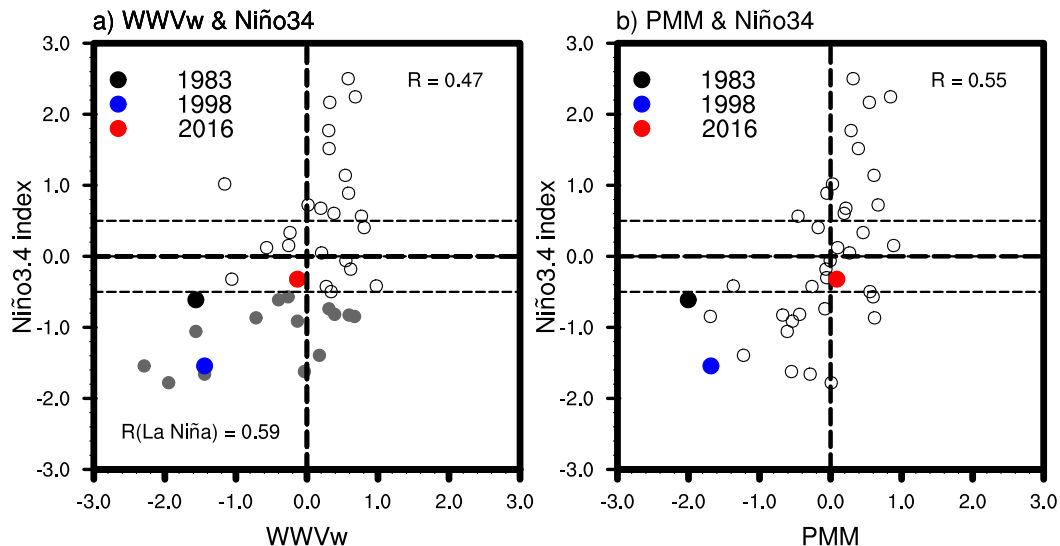
FIG. 13. Scatterplots of the relationship between ENSO amplitude (Niño-3.4 index: 5°S–5°N, 170°W–90°W) at its peak (NDJ) between (a) WWVw (5°S–5°N, 120°E–155°W) 13 months before (i.e., $OND_{Year(-1)}$) (b) and monthly mean PMM wind index during ENSO transition phase (May–June) from 1980 to 2018. The coefficients (R) are labeled in the upper-right corner of the corresponding panel. The coefficient (R) between WWVw and Niño-3.4 index during La Niña years is labeled in the lower-left corner of the corresponding panel.

required to improve our understanding of ENSO dynamics and its prediction.

REFERENCES

Alexander, M. A., I. Bladé, M. Newman, J. R. Lanzante, N.-C. Lau, and J. D. Scott, 2002: The atmospheric bridge: The influence of ENSO teleconnections on air–sea interaction over the global oceans. *J. Climate*, **15**, 2205–2231, https://doi.org/10.1175/1520-0442(2002)015<2205:TABTIO>2.0.CO;2.

——, D. J. Vimont, P. Chang, and J. D. Scott, 2010: The impact of extratropical atmospheric variability on ENSO: Testing the seasonal footprinting mechanism using coupled model experiments. *J. Climate*, **23**, 2885–2901, https://doi.org/10.1175/2010JCLI3205.1.

Amaya, D. J., 2019: The Pacific meridional mode and ENSO: A review. *Curr. Climate Change Rep.*, **5**, 296–307, https://doi.org/10.1007/s40641-019-00142-x.

An, S.-I., 2008: Interannual variations of the tropical ocean instability wave and ENSO. *J. Climate*, **21**, 3680–3686, https://doi.org/10.1175/2008JCLI1701.1.

——, and F.-F. Jin, 2004: Nonlinearity and asymmetry of ENSO. *J. Climate*, **17**, 2399–2412, https://doi.org/10.1175/1520-0442(2004)017<2399:NAAOE>2.0.CO;2.

Anderson, B. T., R. C. Perez, and A. Karspeck, 2013: Triggering of El Niño onset through trade wind–induced charging of the equatorial Pacific. *Geophys. Res. Lett.*, **40**, 1212–1216, https://doi.org/10.1002/grl.50200.

Barnett, T. P., 1983: Interaction of the monsoon and Pacific trade wind system at interannual time scales. Part I: The equatorial zone. *Mon. Wea. Rev.*, **111**, 756–773, https://doi.org/10.1175/1520-0493(1983)111<0756:IOTMAP>2.0.CO;2.

Battisti, D. S., and A. C. Hirst, 1989: Interannual variability in a tropical atmosphere–ocean model: Influence of the basic state, ocean geometry, and nonlinearity. *J. Atmos. Sci.*, **46**, 1687–1712, https://doi.org/10.1175/1520-0469(1989)046<1687:IVIATA>2.0.CO;2.

Baturin, N. G., and P. P. Niiler, 1997: Effects of instability waves in the mixed layer of the equatorial Pacific. *J. Geophys. Res.*, **102**, 27 771–27 793, https://doi.org/10.1029/97JC02455.

Behringer, D., and Y. Xue, 2004: Evaluation of the Global Ocean Data Assimilation System at NCEP: The Pacific Ocean. *Eighth Symp. on Integrated Observing and Assimilation Systems for Atmosphere, Oceans, and Land Surface*, Seattle, WA, Amer. Meteor. Soc., 2.3, https://ams.confex.com/ams/pdfpapers/70720.pdf.

Bjerknes, J., 1969: Atmospheric teleconnections from the equatorial Pacific. *Mon. Wea. Rev.*, **97**, 163–172, https://doi.org/10.1175/1520-0493(1969)097<0163:ATFTEP>2.3.CO;2.

Boucharel, J., and F.-F. Jin, 2020: A simple theory for the modulation of tropical instability waves by ENSO and the annual cycle. *Tellus*, **72**, 1–14, https://doi.org/10.1080/16000870.2019.1700087.

——, A. Timmermann, and F.-F. Jin, 2013: Zonal phase propagation of ENSO sea surface temperature anomalies: Revisited. *Geophys. Res. Lett.*, **40**, 4048–4053, https://doi.org/10.1002/grl.50685.

——, ——, A. Santoso, M. H. England, F.-F. Jin, and M. A. Balmaseda, 2015: A surface layer variance heat budget for ENSO. *Geophys. Res. Lett.*, **42**, 3529–3537, https://doi.org/10.1002/2015GL063843.

Bryden, H. L., and E. C. Brady, 1989: Eddy momentum and heat fluxes and their effects on the circulation of the equatorial Pacific Ocean. *J. Mar. Res.*, **47**, 55–79, https://doi.org/10.1357/002224089785076389.

Cane, M. A., and S. E. Zebiak, 1985: A theory for El Niño and the Southern Oscillation. *Science*, **228**, 1085–1087, https://doi.org/10.1126/science.228.4703.1085.

Chakravorty, S., R. Perez, B. Anderson, B. Giese, S. Larson, and V. Pivotti, 2020: Testing the trade wind charging mechanism and its influence on ENSO variability. *J. Climate*, **33**, 7391–7411, https://doi.org/10.1175/JCLI-D-19-0727.1.

Chang, P., L. Zhang, R. Saravanan, D. J. Vimont, J. C. H. Chiang, L. Ji, H. Seidel, and M. K. Tippett, 2007: Pacific meridional mode and El Niño–Southern Oscillation. *Geophys. Res. Lett.*, **34**, L16608, https://doi.org/10.1029/2007GL030302.

Chen, D., and Coauthors, 2015: Strong influence of westerly wind bursts on El Niño diversity. *Nat. Geosci.*, **8**, 339–345, https://doi.org/10.1038/ngeo2399.

Chiang, J. C. H., and D. J. Vimont, 2004: Analogous Pacific and Atlantic meridional modes of tropical atmosphere–ocean variability. *J. Climate*, **17**, 4143–4158, https://doi.org/10.1175/JCLI4953.1.

Cox, M. D., 1980: Generation and propagation of 30-day waves in a numerical model of the Pacific. *J. Phys. Oceanogr.*, **10**, 1168–1186, https://doi.org/10.1175/1520-0485(1980)010<1168:GAPODW>2.0.CO;2.

Graham, T., 2014: The importance of eddy permitting model resolution for simulation of the heat budget of tropical instability waves. *Ocean Modell.*, **79**, 21–32, https://doi.org/10.1016/j.ocemod.2014.04.005.

Ham, Y.-G., and I.-S. Kang, 2011: Improvement of seasonal forecasts with inclusion of tropical instability waves on initial conditions. *Climate Dyn.*, **36**, 1277–1290, https://doi.org/10.1007/s00382-010-0743-0.

Hansen, D. V., and C. A. Paul, 1984: Genesis and effects of long waves in the equatorial Pacific. *J. Geophys. Res.*, **89**, 10 431–10 440, https://doi.org/10.1029/JC089iC06p10431.

Harrison, D. E., and G. A. Vecchi, 1999: On the termination of El Niño. *Geophys. Res. Lett.*, **26**, 1593–1596, https://doi.org/10.1029/1999GL900316.

Hersbach, H., and D. Dee, 2016: ERA5 reanalysis is in production. *ECMWF Newsletter*, No. 147, ECMWF, Reading, United Kingdom, 7, https://www.ecmwf.int/en/newsletter/147/news/era5-reanalysis-production.

Holmes, R. M., and L. N. Thomas, 2016: Modulation of tropical instability wave intensity by equatorial Kelvin waves. *J. Phys. Oceanogr.*, **46**, 2623–2643, https://doi.org/10.1175/JPO-D-16-0064.1.

——, S. McGregor, A. Santoso, and M. H. England, 2019: Contribution of tropical instability waves to ENSO irregularity. *Climate Dyn.*, **52**, 1837–1855, https://doi.org/10.1007/s00382-018-4217-0.

Hu, S., and A. V. Fedorov, 2016: Exceptionally strong easterly wind burst stalling El Niño of 2014. *Proc. Natl. Acad. Sci. USA*, **113**, 2005–2010, https://doi.org/10.1073/pnas.1514182113.

——, and ——, 2019: The extreme El Niño of 2015–2016: The role of westerly and easterly wind bursts, and preconditioning by the failed 2014 event. *Climate Dyn.*, **52**, 7339–7357, https://doi.org/10.1007/s00382-017-3531-2.

Huang, B., Y. Xue, D. Zhang, A. Kumar, and M. J. McPhaden, 2010: The NCEP GODAS ocean analysis of the tropical Pacific mixed layer heat budget on seasonal to interannual time scales. *J. Climate*, **23**, 4901–4925, https://doi.org/10.1175/2010JCLI3373.1.

——, and Coauthors, 2017: Extended Reconstructed Sea Surface Temperature, version 5 (ERSSTv5): Upgrades, validations, and intercomparisons. *J. Climate*, **30**, 8179–8205, https://doi.org/10.1175/JCLI-D-16-0836.1.

Im, S.-H., S.-I. An, M. Lengaigne, and Y. Noh, 2012: Seasonality of tropical instability waves and its feedback to the seasonal cycle in the tropical eastern Pacific. *Sci. World J.*, **2012**, 1–11, https://doi.org/10.1100/2012/612048.

Imada, Y., and M. Kimoto, 2012: Parameterization of tropical instability waves and examination of their impact on ENSO characteristics. *J. Climate*, **25**, 4568–4581, https://doi.org/10.1175/JCLI-D-11-00233.1.

Jin, F.-F., 1997a: An equatorial ocean recharge paradigm for ENSO. Part I: Conceptual model. *J. Atmos. Sci.*, **54**, 811–829, https://doi.org/10.1175/1520-0469(1997)054<0811:AEORPF>2.0.CO;2.

——, 1997b: An equatorial ocean recharge paradigm for ENSO. Part II: A stripped-down coupled model. *J. Atmos. Sci.*, **54**, 830–847, https://doi.org/10.1175/1520-0469(1997)054<0830:AEORPF>2.0.CO;2.

——, S.-I. An, A. Timmermann, and J. Zhao, 2003: Strong El Niño events and nonlinear dynamical heating. *Geophys. Res. Lett.*, **30**, 1120, https://doi.org/10.1029/2002GL016356.

Jochum, M., and R. Murtugudde, 2006: Temperature advection by tropical instability waves. *J. Phys. Oceanogr.*, **36**, 592–605, https://doi.org/10.1175/JPO2870.1.

——, M. F. Cronin, W. S. Kessler, and D. Shea, 2007: Observed horizontal temperature advection by tropical instability waves. *Geophys. Res. Lett.*, **34**, L09604, https://doi.org/10.1029/2007GL029416.

Kakatkar, R., C. Gnanaseelan, J. S. Deepa, J. Chowdary, and A. Parekh, 2018: Role of ocean–atmosphere interactions in modulating the 2016 La Niña like pattern over the tropical Pacific. *Dyn. Atmos. Oceans*, **83**, 100–110, https://doi.org/10.1016/j.dynatmoce.2018.07.003.

Latif, M., and Coauthors, 2001: ENSIP: The El Niño Simulation Intercomparison Project. *Climate Dyn.*, **18**, 255–276, https://doi.org/10.1007/s003820100174.

Legeckis, R., 1977: Long waves in the eastern equatorial Pacific Ocean: A view from a geostationary satellite. *Science*, **197**, 1179–1181, https://doi.org/10.1126/science.197.4309.1179.

Lengaigne, M., J.-P. Boulanger, P. Delecluse, C. Menkes, E. Guilyardi, and J. Slingo, 2004: Westerly wind events in the tropical Pacific and their influence on the coupled ocean–atmosphere system: A review. *Earth's Climate: The Ocean–Atmosphere Interaction, Geophys. Monogr.*, Vol. 147, Amer. Geophys. Union, 49–69, https://doi.org/10.1029/147GM03.

Levine, A. F. Z., and M. J. McPhaden, 2016: How the July 2014 easterly wind burst gave the 2015–2016 El Niño a head start. *Geophys. Res. Lett.*, **43**, 6503–6510, https://doi.org/10.1002/2016GL069204.

L'Heureux, M. L., and Coauthors, 2017: Observing and predicting the 2015/16 El Niño. *Bull. Amer. Meteor. Soc.*, **98**, 1363–1382, https://doi.org/10.1175/BAMS-D-16-0009.1.

Li, X., Z.-Z. Hu, and B. Huang, 2019: Contributions of atmosphere–ocean interaction and low-frequency variation to intensity of strong El Niño events since 1979. *J. Climate*, **32**, 1381–1394, https://doi.org/10.1175/JCLI-D-18-0209.1.

Lim, E.-P., and H. H. Hendon, 2017: Causes and predictability of the negative Indian Ocean dipole and its impact on La Niña during 2016. *Sci. Rep.*, **7**, 12619, https://doi.org/10.1038/s41598-017-12674-z.

Lim, Y.-K., R. M. Kovach, S. Pawson, and G. Vernieres, 2017: The 2015/16 El Niño event in context of the MERRA-2 reanalysis:

A comparison of the tropical Pacific with 1982/83 and 1997/98. *J. Climate*, **30**, 4819–4842, https://doi.org/10.1175/JCLI-D-16-0800.1.

Lyman, J. M., G. C. Johnson, and W. S. Kessler, 2007: Distinct 17- and 33-day tropical instability waves in subsurface observations. *J. Phys. Oceanogr.*, **37**, 855–872, https://doi.org/10.1175/JPO3023.1.

Masina, S., and S. G. H. Philander, 1999: An analysis of tropical instability waves in a numerical model of the Pacific Ocean: 1. Spatial variability of the waves. *J. Geophys. Res.*, **104**, 29 613–29 635, https://doi.org/10.1029/1999JC900227.

——, ——, and A. B. G. Bush, 1999: An analysis of tropical instability waves in a numerical model of the Pacific Ocean: 2. Generation and energetics of the waves. *J. Geophys. Res.*, **104**, 29 637–29 661, https://doi.org/10.1029/1999JC900226.

McGregor, S., N. Ramesh, P. Spence, M. H. England, M. J. McPhaden, and A. Santoso, 2013: Meridional movement of wind anomalies during ENSO events and their role in event termination. *Geophys. Res. Lett.*, **40**, 749–754, https://doi.org/10.1002/grl.50136.

McPhaden, M. J., S. E. Zebiak, and M. H. Glantz, 2006: ENSO as an integrating concept in Earth science. *Science*, **314**, 1740–1745, https://doi.org/10.1126/science.1132588.

Meinen, C. S., and M. J. McPhaden, 2000: Observations of warm water volume changes in the equatorial Pacific and their relationship to El Niño and La Niña. *J. Climate*, **13**, 3551–3559, https://doi.org/10.1175/1520-0442(2000)013<3551:OOWWVC>2.0.CO;2.

Menkes, C. E., J. G. Vialard, S. C. Kennan, J.-P. Boulanger, and G. V. Madec, 2006: A modeling study of the impact of tropical instability waves on the heat budget of the eastern equatorial Pacific. *J. Phys. Oceanogr.*, **36**, 847–865, https://doi.org/10.1175/JPO2904.1.

——, M. Lengaigne, J. Vialard, M. Puy, P. Marchesiello, S. Cravatte, and G. Cambon, 2014: About the role of westerly wind events in the possible development of an El Niño in 2014. *Geophys. Res. Lett.*, **41**, 6476–6483, https://doi.org/10.1002/2014GL061186.

Min, Q., J. Su, R. Zhang, and X. Rong, 2015: What hindered the El Niño pattern in 2014? *Geophys. Res. Lett.*, **42**, 6762–6770, https://doi.org/10.1002/2015GL064899.

——, ——, and ——, 2017: Impact of the South and North Pacific meridional modes on the El Niño–Southern Oscillation: Observational analysis and comparison. *J. Climate*, **30**, 1705–1720, https://doi.org/10.1175/JCLI-D-16-0063.1.

Miyakawa, T., H. Yashiro, T. Suzuki, H. Tatebe, and M. Satoh, 2017: A Madden–Julian oscillation event remotely accelerates ocean upwelling to abruptly terminate the 1997/1998 super El Niño. *Geophys. Res. Lett.*, **44**, 9489–9495, https://doi.org/10.1002/2017GL074683.

North, G. R., T. L. Bell, R. F. Cahalan, and F. J. Moeng, 1982: Sampling errors in the estimation of empirical orthogonal functions. *Mon. Wea. Rev.*, **110**, 699–706, https://doi.org/10.1175/1520-0493(1982)110<0699:SEITEO>2.0.CO;2.

Paek, H., J.-Y. Yu, and C. Qian, 2017: Why were the 2015/2016 and 1997/1998 extreme El Niños different? *Geophys. Res. Lett.*, **44**, 1848–1856, https://doi.org/10.1002/2016GL071515.

Philander, S. G. H., 1976: Instabilities of zonal equatorial currents. *J. Geophys. Res.*, **81**, 3725–3735, https://doi.org/10.1029/JC081i021p03725.

Picaut, J., 1997: An advective-reflective conceptual model for the oscillatory nature of the ENSO. *Science*, **277**, 663–666, https://doi.org/10.1126/science.277.5326.663.

Planton, Y., J. Vialard, E. Guilyardi, M. Lengaigne, and T. Izumo, 2018: Western Pacific oceanic heat content: A better predictor

of La Niña than of El Niño. *Geophys. Res. Lett.*, **45**, 9824–9833, https://doi.org/10.1029/2018GL079341.

Proehl, J. A., 1996: Linear stability of equatorial zonal flows. *J. Phys. Oceanogr.*, **26**, 601–621, https://doi.org/10.1175/1520-0485(1996)026<0601:LSOEZF>2.0.CO;2.

Qiao, L., and R. H. Weisberg, 1995: Tropical instability wave kinematics: Observations from the tropical instability wave experiment. *J. Geophys. Res.*, **100**, 8677, https://doi.org/10.1029/95JC00305.

Rasmusson, E. M., and T. H. Carpenter, 1982: Variations in tropical sea surface temperature and surface wind fields associated with the southern oscillation/El Niño. *Mon. Wea. Rev.*, **110**, 354–384, https://doi.org/10.1175/1520-0493(1982)110<0354:VITSST>2.0.CO;2.

Reynolds, R. W., N. A. Rayner, T. M. Smith, D. C. Stokes, and W. Wang, 2002: An improved in situ and satellite SST analysis for climate. *J. Climate*, **15**, 1609–1625, https://doi.org/10.1175/1520-0442(2002)015<1609:AIISAS>2.0.CO;2.

Ropelewski, C. F., and M. S. Halpert, 1987: Global and regional scale precipitation patterns associated with the El Niño/Southern Oscillation. *Mon. Wea. Rev.*, **115**, 1606–1626, https://doi.org/10.1175/1520-0493(1987)115<1606:GARSPP>2.0.CO;2.

——, and ——, 1996: Quantifying Southern Oscillation–precipitation relationships. *J. Climate*, **9**, 1043–1059, https://doi.org/10.1175/1520-0442(1996)009<1043:QSOPR>2.0.CO;2.

Santoso, A., M. J. McPhaden, and W. Cai, 2017: The defining characteristics of ENSO extremes and the strong 2015/2016 El Niño. *Rev. Geophys.*, **55**, 1079–1129, https://doi.org/10.1002/2017RG000560.

Seiki, A., and Y. N. Takayabu, 2007: Westerly wind bursts and their relationship with intraseasonal variations and ENSO. Part I: Statistics. *Mon. Wea. Rev.*, **135**, 3325–3345, https://doi.org/10.1175/MWR3477.1.

Shinoda, T., G. N. Kiladis, and P. E. Roundy, 2009: Statistical representation of equatorial waves and tropical instability waves in the Pacific Ocean. *Atmos. Res.*, **94**, 37–44, https://doi.org/10.1016/j.atmosres.2008.06.002.

Su, J., B. Xiang, B. Wang, and T. Li, 2014: Abrupt termination of the 2012 Pacific warming and its implication on ENSO prediction. *Geophys. Res. Lett.*, **41**, 9058–9064, https://doi.org/10.1002/2014GL062380.

——, R. Zhang, X. Rong, Q. Min, and C. Zhu, 2018: Sea surface temperature in the subtropical Pacific boosted the 2015 El Niño and hindered the 2016 La Niña. *J. Climate*, **31**, 877–893, https://doi.org/10.1175/JCLI-D-17-0379.1.

Suarez, M. J., and P. S. Schopf, 1988: A delayed action oscillator for ENSO. *J. Atmos. Sci.*, **45**, 3283–3287, https://doi.org/10.1175/1520-0469(1988)045<3283:ADAOFE>2.0.CO;2.

Timmermann, A., and Coauthors, 2018: El Niño–Southern Oscillation complexity. *Nature*, **559**, 535–545, https://doi.org/10.1038/s41586-018-0252-6.

Trenberth, K. E., and J. M. Caron, 2000: The Southern Oscillation revisited: Sea level pressures, surface temperatures, and precipitation. *J. Climate*, **13**, 4358–4365, https://doi.org/10.1175/1520-0442(2000)013<4358:TSORSL>2.0.CO;2.

van Loon, H., and R. A. Madden, 1981: The Southern Oscillation. Part I: Global associations with pressure and temperature in northern winter. *Mon. Wea. Rev.*, **109**, 1150–1162, https://doi.org/10.1175/1520-0493(1981)109<1150:TSOPIG>2.0.CO;2.

Vecchi, G. A., 2006: The termination of the 1997–98 El Niño. Part II: Mechanisms of atmospheric change. *J. Climate*, **19**, 2647–2664, https://doi.org/10.1175/JCLI3780.1.

——, and D. E. Harrison, 2003: On the termination of the 2002–03 El Niño event. *Geophys. Res. Lett.*, **30**, 1964, https://doi.org/10.1029/2003GL017564.

——, and ——, 2006: The termination of the 1997–98 El Niño. Part I: Mechanisms of oceanic change. *J. Climate*, **19**, 2633–2646, https://doi.org/10.1175/JCLI3776.1.

Vialard, J., C. Menkes, J.-P. Boulanger, P. Delecluse, E. Guilyardi, M. J. McPhaden, and G. Madec, 2001: A model study of oceanic mechanisms affecting equatorial Pacific sea surface temperature during the 1997–98 El Niño. *J. Phys. Oceanogr.*, **31**, 1649–1675, https://doi.org/10.1175/1520-0485(2001)031<1649:AMSOOM>2.0.CO;2.

Vimont, D. J., D. S. Battisti, and A. C. Hirst, 2001: Footprinting: A seasonal connection between the tropics and mid-latitudes. *Geophys. Res. Lett.*, **28**, 3923–3926, https://doi.org/10.1029/2001GL013435.

——, ——, and ——, 2003a: The seasonal footprinting mechanism in the CSIRO general circulation models. *J. Climate*, **16**, 2653–2667, https://doi.org/10.1175/1520-0442(2003)016<2653:TSFMIT>2.0.CO;2.

——, J. M. Wallace, and D. S. Battisti, 2003b: The seasonal footprinting mechanism in the Pacific: Implications for ENSO. *J. Climate*, **16**, 2668–2675, https://doi.org/10.1175/1520-0442(2003)016<2668:TSFMIT>2.0.CO;2.

Wallace, J. M., E. M. Rasmusson, T. P. Mitchell, V. E. Kousky, E. S. Sarachik, and H. von Storch, 1998: On the structure and evolution of ENSO-related climate variability in the tropical Pacific: Lessons from TOGA. *J. Geophys. Res.*, **103**, 14 241–14 259, https://doi.org/10.1029/97JC02905.

Wang, M., S.-P. Xie, S. Shen, and Y. Du, 2020: Rossby and Yanai modes of tropical instability waves in the equatorial Pacific Ocean and a diagnostic model for surface currents. *J. Phys. Oceanogr.*, **50**, 3009–3024, https://doi.org/10.1175/JPO-D-20-0063.1.

Wang, W., and M. J. McPhaden, 1999: The surface-layer heat balance in the equatorial Pacific Ocean. Part I: Mean seasonal cycle. *J. Phys. Oceanogr.*, **29**, 1812–1831, https://doi.org/10.1175/1520-0485(1999)029<1812:TSLHBI>2.0.CO;2.

——, and ——, 2001: Surface layer temperature balance in the equatorial Pacific during the 1997–98 El Niño and 1998–99 La Niña. *J. Climate*, **14**, 3393–3407, https://doi.org/10.1175/1520-0442(2001)014<3393:SLTBIT>2.0.CO;2.

Weisberg, R. H., and T. J. Weingartner, 1988: Instability waves in the equatorial Atlantic Ocean. *J. Phys. Oceanogr.*, **18**, 1641–1657, https://doi.org/10.1175/1520-0485(1988)018<1641:IWITEA>2.0.CO;2.

——, and C. Wang, 1997: A western Pacific oscillator paradigm for the El Niño-southern oscillation. *Geophys. Res. Lett.*, **24**, 779–782, https://doi.org/10.1029/97GL00689.

Wheeler, M. C., and H. H. Hendon, 2004: An all-season real-time multivariate MJO index: Development of an index for monitoring and prediction. *Mon. Wea. Rev.*, **132**, 1917–1932, https://doi.org/10.1175/1520-0493(2004)132<1917:AARMMI>2.0.CO;2.

Wilson, D., and A. Leetmaa, 1988: Acoustic Doppler current profiling in the equatorial Pacific in 1984. *J. Geophys. Res.*, **93**, 13 947–13 966, https://doi.org/10.1029/JC093iC11p13947.

Wu, Q., and K. P. Bowman, 2007: Interannual variations of tropical instability waves observed by the Tropical Rainfall Measuring Mission. *Geophys. Res. Lett.*, **34**, L09701, https://doi.org/10.1029/2007GL029719.

Wu, Y.-K., L. Chen, C.-C. Hong, T. Li, C.-T. Chen, and L. Wang, 2018: Role of the meridional dipole of SSTA and associated cross-equatorial flow in the tropical eastern Pacific in terminating the 2014 El Niño development. *Climate Dyn.*, **50**, 1625–1638, https://doi.org/10.1007/s00382-017-3710-1.

Xue, A., F.-F. Jin, W. Zhang, J. Boucharel, S. Zhao, and X. Yuan, 2020: Delineating the seasonally modulated nonlinear feedback onto ENSO from tropical instability waves. *Geophys. Res. Lett.*, **47**, e2019GL085863, https://doi.org/10.1029/2019GL085863.

Yu, J.-Y., and W. T. Liu, 2003: A linear relationship between ENSO intensity and tropical instability wave activity in the eastern Pacific Ocean. *Geophys. Res. Lett.*, **30**, 1735, https://doi.org/10.1029/2003GL017176.

Yu, Z., J. P. McCreary, and J. A. Proehl, 1995: Meridional asymmetry and energetics of tropical instability waves. *J. Phys. Oceanogr.*, **25**, 2997–3007, https://doi.org/10.1175/1520-0485(1995)025<2997:MAAEOT>2.0.CO;2.

Zhang, H., A. Clement, and P. Di Nezio, 2014a: The South Pacific meridional mode: A mechanism for ENSO-like variability. *J. Climate*, **27**, 769–783, https://doi.org/10.1175/JCLI-D-13-00082.1.

——, C. Deser, A. Clement, and R. Tomas, 2014b: Equatorial signatures of the Pacific meridional modes: Dependence on mean climate state. *Geophys. Res. Lett.*, **41**, 568–574, https://doi.org/10.1002/2013GL058842.

Zheng, F., L. Feng, and J. Zhu, 2015: An incursion of off-equatorial subsurface cold water and its role in triggering the "double dip" La Niña event of 2011. *Adv. Atmos. Sci.*, **32**, 731–742, https://doi.org/10.1007/s00376-014-4080-9.

Zhu, J., A. Kumar, B. Huang, M. A. Balmaseda, Z.-Z. Hu, L. Marx, and J. L. Kinter Iii, 2016: The role of off-equatorial surface temperature anomalies in the 2014 El Niño prediction. *Sci. Rep.*, **6**, 19677, https://doi.org/10.1038/srep19677.